地上重力下における多種微粒子含有プラズマの構造と運動の観察

○盛林高志, 増田理沙, 三重野哲（静岡大）, 林康明（京都工繊維大）

Observation of Structures and Motions in the Plasma with Size-Distributed Fine Particles under the Ground Gravity

○Takashi MORIBAYASHI, Risa MASUDA, Tetsu MIENO (Shizuoka Univ.),
Yasuaki HAYASHI (Kyoto Inst. Technol.)

Related with complex systems, fine-particle plasmas have much attention to scientists and engineers [1,2]. Hence, we are making crystal-like structures by using a high-frequency (HF) Ar plasma, and try to analyze structures and motions of charged particles under the ground gravity. Schematic of the developed plasma machine is shown in Fig. 1. In a stainless steel chamber (150 mmφ, 150 mmh), a 100 mmφ disk electrode and a 80 mmφ metal ring are set. In this experiment, HF argon discharge (100kHz) is produced at 10~13 Pa by applying HF voltage of about 270~290 V_{rms} to the mesh electrode with respect to the upper grounded electrode. And the ring was set on the lower electrode to confine fine-particles. The cloud diffuses under the upper electrode.

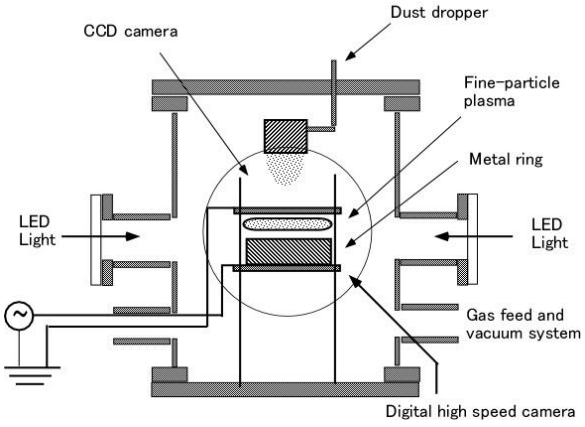

Fig.1 Schematic arrangement of experimental setup.

The particles used are silicon nitride which have diameter of $d \simeq 1$ μm. They were injected from a dust dropper. A digital high speed camera and a CCD video camera are used to investigate the particle behaviors. Under discharge voltage V_d= 280 V_{rm}, discharge current I_d= 0.2 A_{rm} and the pressure p(Ar) = 13 Pa, a disk-shaped cloud is generated as shown in Fig.2. The expanded image is shown in Fig.3. There is a stable 3D structure, in which particles are vibrating. The bigger particles tend to accumulate at the edge of cloud.

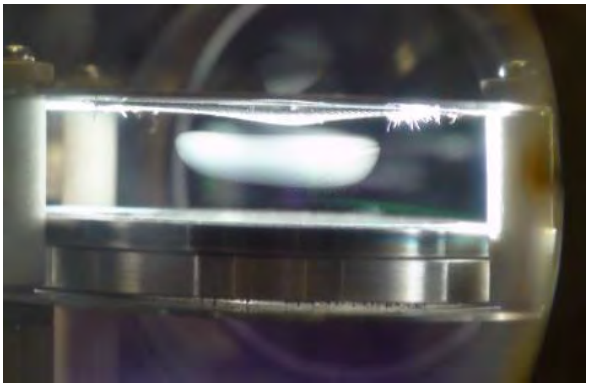

Fig.2 The disk-shaped cloud of Si_3N_4 in the HF Ar plasma. V_{RF}=280V_{rms}, I_{RF}=0.2A_{rms}, f=100kHz, p(Ar)=13Pa.

Fig.3 Solid structure (profile) by charged particles in the plasma.

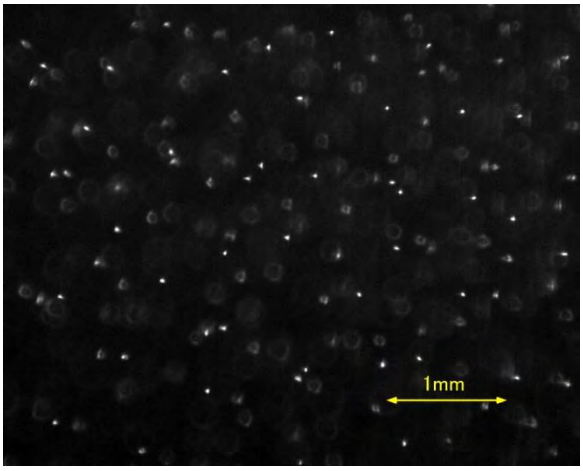

References

[1] Y. Hayashi, K. Tachibana, J. Vac. Sci. Technol. **A 14(2)**, Mar/Apr 1996, 506.

[2] H. Thomas, G.E. Morfill, V. Demmel, Phys. Rev. Lett. **73**, 1994, 652.

P02

無容器プロセスを用いた$(In_{1-x}Ga_x)Sb$Ⅲ-Ⅴ族混晶半導体の過冷度と微細構造

○河村 忠晴, 永山 勝久（芝浦工大）

Undercooling and Microstructure of $(In_{1-x}Ga_x)Sb$ Ⅲ-Ⅴ Semiconductor Alloys by using Containerless Solidification Process

○Tadaharu KAWAMURA[1] and Katsuhisa NAGAYAMA[2]
[1]Graduate Student, Shibaura Institute of Technology
[2]Department of Materials Science, Faculty of Engineering, Shibaura Institute of Technology

1. Introduction

Semiconductor alloys was known as a semiconductor material continuously a various the lattice constant and band gap depending on the composition ratio, the production of the bulk in the homogeneous composition was difficult from the effects of segregation and convection on the gravity. We've reported on the relationship of crystal growth and the undercooling degree of InSb and GaSb particles by using the short drop tube process (free fall section 2.5m).

In this study, we have investigated the formation of III-V type semiconductor and semiconductor alloy was prepared fine particles by using the drop tube process.

In addition, we have investigated the relationship of the undercooling degree and the crystal growth of III-V type semiconductor by using electromagnetic levitation process.

2. Experimental

$(In_{1-x}Ga_x)Sb$ (x=0,0.1,0.2,0.3,0.4,0.5,1) alloys was set into the quartz nozzle. The alloy in the quartz nozzle was heating and melting by electromagnetic levitation coil. Free fall tube in this apparatus was evacuated by turbomolecular pump to high vacuum before filling He 1atm atmosphere. The molten sample was dropped by He gas pressure from upperside of the quartz nozzle, and solidified with containerless.

The structure of the solidified sample was examined by X-ray diffractometer (XRD) using CuKα radiation. The microstructure of solidified sample was observed by Field-emission scanning electron microscope (FE-SEM), in detail.

3. Results and Discussions

Fig.1 shows the X-ray patterns of InSb(a), $(In_{0.6}Ga_{0.4})Sb$(b) and GaSb(c) fine particle samples by drop tube solidified. The diffraction peaks of the ternary samples were observed in the middle range of the InSb compound phase and GaSb compound phase.

Fig.2 shows the summarizing the result of XRD measurement of $(In_{1-x}Ga_x)Sb$ (x=0,0.1,0.2,0.3,0.4,0.5,1) semiconductor alloys. The vertical axis was shown the lattice constant and the horizontal axis was shown x (Ga composition). In this results, the lattice constant is continuously changed by increases of x.

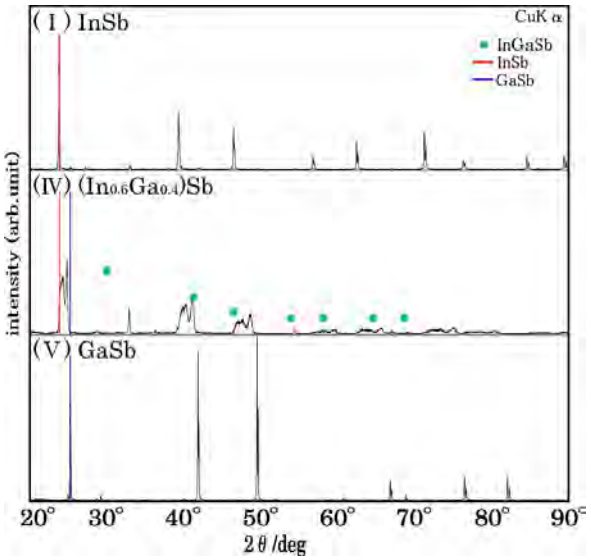

Fig.1 XRD patterns of $(In_{1-x}Ga_x)Sb$ (x=0,0.4,1)

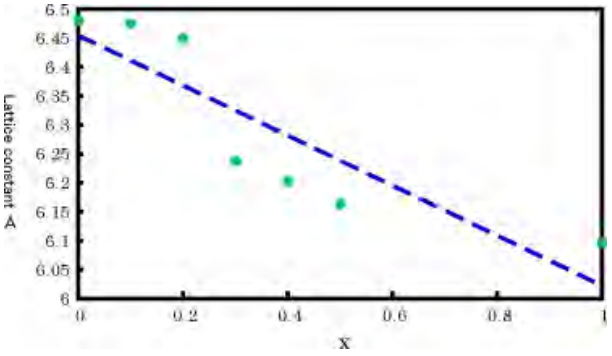

Fig.2 Relationship of the composition ratio and lattice constant

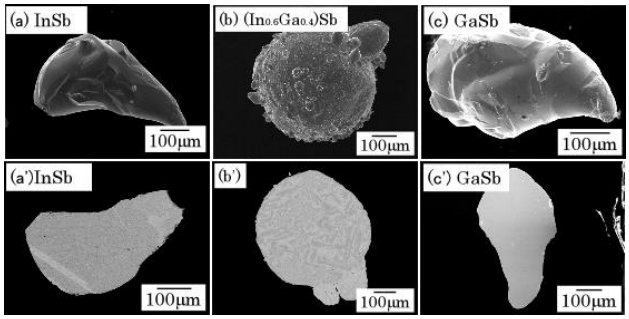

Fig.3 SEM images of the surface and microstructure of (a)InSb, (b)$(In_{0.6}Ga_{0.4})Sb$ and (c)GaSb

Fig.3 shows the SEM images of surface and microstructure of InSb(a), $(In_{0.6}Ga_{0.4})Sb$(b) and GaSb(c) fine particle sample. Binary sample of InSb(a) and GaSb(c) was formed sharp projection by solidification expansion. The surface morphology was indicated a lateral growth may be attributed to the low undercooling solidification.

However, ternary samples of $(In_{1-x}Ga_x)Sb$ were formed a lot of sample surface. It was shown the fine surface by dendritic structure formation may be attributed to the high undercooling solidification.

Also, the binary sample was composed of several crystal grains in the low degree of undercooling sample, especially. On the other hand, ternary sample was polycrystalline structure for almost all samples were solidified in the high undercooling.

Fig.4 shows the SEM image of microstructure of the $(In_{0.6}Ga_{0.4})Sb$ sample. $(In_{0.3}Ga_{0.7})Sb$ phase crystallized as the primary crystal and InSb phase crystallized as the second phase. Also, the grain boundary was formed segregated In.

The composition ratio of the primary phase also continuously changed with changing the composition ratio of the $(In_{1-x}Ga_x)Sb$ alloys.

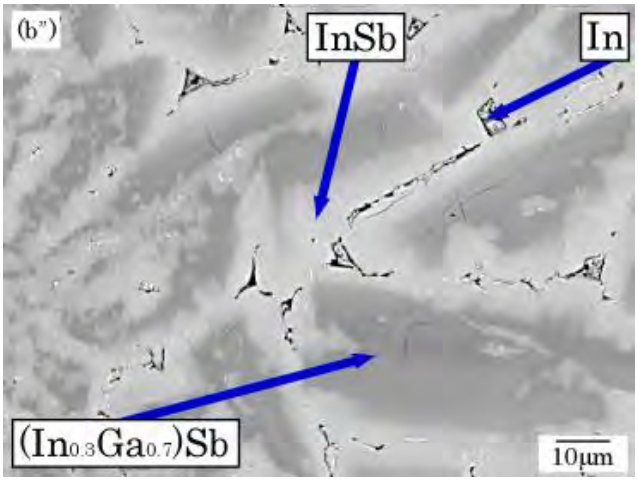

Fig.4 SEM images of the microstructure of the $(In_{0.6}Ga_{0.4})Sb$.

P03

音場浮遊液滴の浮遊安定性に関する基礎的検討

○河野健吾，長谷川浩司，大竹浩靖（工学院大），合田篤（筑波大院），阿部豊（筑波大）

Experimental Investigation of Levitation Stability of an Acoustically Levitated Droplet

○Kengo KONO, Koji HASEGAWA , Hiroyasu OHTAKE (Kogakuin Univ.)
Atsushi GODA, Yutaka ABE (University of Tsukuba)

1. Introduction

Acoustic levitation method is studied to apply to manufacturing new materials in the microgravity condition, fluid transportation in the chemical and medical field[1]. However, this method causes the translational motion and interfacial behavior of droplet arises from that acoustic radiation pressure acting on its surface[2]. These non-linear behavior bring about the negative effect on the quality of materials and fluid manipulation. With the flat type reflector, it is necessary to increase the sound pressure in the test section in order to improve the holding force of levitated droplet, thus, translational motion and interfacial behavior are even more noticeable. Meanwhile, Xie et al.[4] numerically investigated and showed that it can be improved levitation stability and restoring force on the droplet with concave reflector. However, the experimental findings about levitation stability and restoring force with concave reflector is not enough. We have developed acoustic levitation system including concave reflector and experimentally investigated translational motion and sound pressure distribution in the test section[5].

As mentioned above, it is important to clarify the non-linear effect and dynamic motion acting on a levitated droplet and achieve the stable fluid manipulation. Purpose of our study is to find out the generating mechanism of translational motion and interfacial behavior (atomization) acting on the levitated droplet and improve the levitation stability of the droplet.

2. Experimental apparatus

2.1 Experimental procedure and conditions

The experimental systems are composed of the test section, ultrasonic transmission unit and observation unit. First, we transmit sinusoidal signal using the function generator and amplification it using the power amplifier. Then this is inputted to the ultrasonic transducer through the power meter and sound wave is generated from the bottom horn and it reflects on the top reflector. Acoustic standing wave is formed between horn and reflector and the droplet is injected using syringe in manual operation. Droplet levitates near the node of the acoustic standing wave. To observe behavior of levitated droplet, we recorded levitated droplet by backlight method using high speed video camera and processed the obtained image using computer and application.

Test sample is pure water. Diameter of droplet d is calculated by assuming as spheroid. Aspect ratio b/a is derived by the ratio of the major axis b to the minor axis a. The distance between the horn and reflector is approximately 49 mm. Shutter speed is 4000fps with spatial resolution of 47±1 μm/pixel.

2.2 Geometry of reflector

In this study, we used two different types of reflectors shown in **Fig. 1**. The flat type and the concave type are $R=\infty$ (below, R∞) and R=36 (below, R36), respectively. Curvature configuration of the reflector is shown that $R \fallingdotseq 2\lambda$ is the best configuration to inhibit trans rational motion of the levitated droplet by Xie et al.[4]. In this paper, we investigated the effect of the geometry of the reflector on the behavior of the droplet.

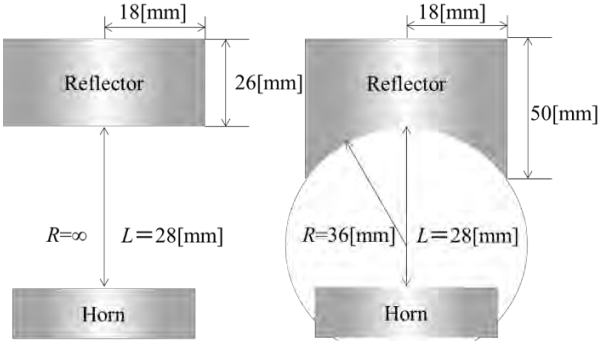

(a) Flat type ($R=\infty$) **(b)** Concave type (R=36mm)

Fig. 1 Geometry of each reflector

Table 1 Experimental conditions

Input frequency [kHz]	19.36
Input power [W]	8.9-55.0
Test sample	Water
Tenparature [℃]	25.5±1.3
Humidity [%]	68.9±5
Equivarent diameter d [mm]	0.3-4.7
Aspect ratio [-]	1.0-3.2

3. Translational motion of levitated droplet

Fig. 2 is translational motion with each reflector. Horizontal axis is time, vertical axis is translational amplitude. It is shown that translational amplitude with R36 is smaller than that with R∞. It is assumed that R36 changed the sound pressure distribution acting on the levitated droplet surface due to the geometric configuration. As a result, it is considered that R36 suppressed the translational amplitude than that with R∞. It is necessary to measure the acoustic pressure distribution at the test section in the state of droplet levitating.

4. Behavior of atomization of water droplet

Fig. 3 shows the droplet atomization process and image. **Fig. 3(a)** is the time series of aspect ratio with the two different droplets. Horizontal axis is time, vertical axis is aspect ratio. Both droplets caused the atomization eventually with rapid deformation of its interface within last 3 ms. Droplet atomized at t = 0 ms. **Fig. 3(b)** is the image of just before the atomization of water droplet showed in **Fig. 3(a)** which its equivalent diameter is 1.6mm. As shown in red square in the image, the interfacial deformation was observed and then atomized from the right and left edge of surface. In the theoretical investigation by Danilov et al.[3], it is indicated that the critical aspect ratio is approximately 8.5. However, the critical aspect ratio is different in our study, and also depends on the droplet size. It is considered that the spatial and temporal resolution are not enough yet, and will be required to improve observation system.

5. Concluding remarks

In the present study, we experimentally investigated about the generating mechanism of translational motion and interfacial behavior (atomization). The following can be acquired;

1. It is shown that translational amplitude with R36 is smaller than that with R∞.
2. Droplets caused the atomization eventually with rapid deformation of its interface within last 3 ms and atomized from the right and left edge of surface. In our study, the critical aspect ratio is different from previous work[3] and also depends on the droplet size.

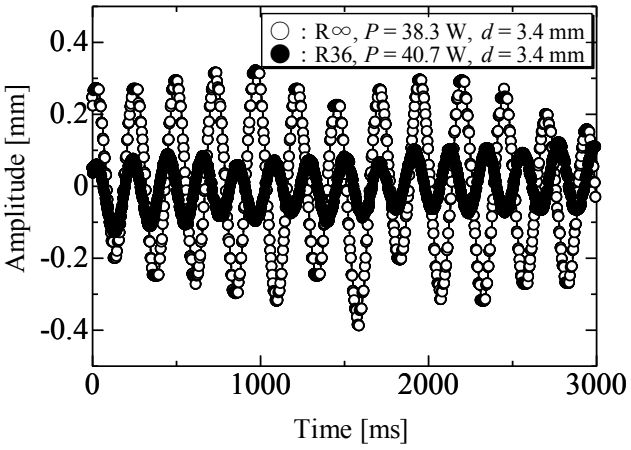

Fig. 2 Translational motion of droplet with each reflector

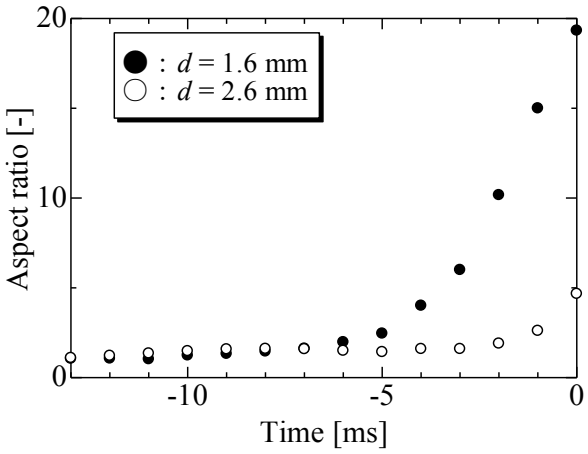

(a) Time series of aspect ratio

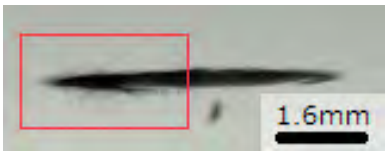

(b) Atomization of water droplet (d=1.6mm, t = 0 ms)

Fig. 3 Interfacial instability on the levitated water droplet

References

1) Foresti, D., Nabavi, M., Klingauf, M., Klingauf, Ferrari, A. and Poulikakos, D., Acoustophoretic contactless transport and handling of matter in air, proceedings of the National Academy of Sciences, **Vol. 110**, No.32, (2013), 12549.

2) Foresti, D., Nabavi, M. and Poulikakos, D., On the Acoustic Levitation Stability Behavior of Spherical and Ellipsoidal Particles, J. Fluid Mech., **Vol. 709**, (2012), 581.

3) Danilov, S. and Mironov, M., Breakup of a Droplet in a High-intensity Sound Fields, J. Acoust. Soc. Am., **Vol. 92**, (1992), 2747.

4) Xie, W. J. and Wei, B., Dependence of Acoustic Levitation Capabilities on Geometric Parameters, Physical Review E, **Vol. 66**, 026605, (2002), 1.

5) Hasegawa, K., et.al., Generation Mechanism of Horizontal Holding Force of an Acoustically Levitated Droplet, Progress in Multiphase Flow Research, **Vol. 27**, No. 5, (2014), 563.

非共溶性混合媒体の核沸騰熱伝達特性に関する研究

○喜多祥太，岩田圭介，新本康久，大田治彦（九州大学）

Boiling Heat Transfer by Nucleate Boiling of Immiscible Mixtures

○Shota KITA, Keisuke IWATA, Yasuhisa SHINMOTO, Haruhiko OHTA (Kyushu Univ.)

1. Introduction

By the development of electronic technology, the heat generation density from semiconductors is increasing. It holds true for the space electronic devices in near future. Liquid cooling systems utilizing the latent heat transportation by nucleate boiling heat transfer have more advantages than the cooling by single-phase liquid.

In pool boiling experiments, an optimized combination of two components with different saturation temperatures and liquid densities improves heat transfer characteristics [1]. For example, critical heat flux(CHF) values for FC72/Water at near optimized layer thicknesses of FC72 before heating are far higher than that for pure water under the same system pressure because of high subcooling condition of water resulted from the compression effect by the high vapor partial pressure of FC72. In addition, the surface temperature in the high heat flux regime is clearly reduced from the pure water. Furthermore, in the presence of the fluctuation of thermal load for practical cooling systems like automobiles, the stability of surface temperature is improved because FC72 accumulated on the heating surface is used at the boiling incipience. This paper reports new experimental data of boiling heat transfer by using immiscible mixtures.

2. Experimental apparatus

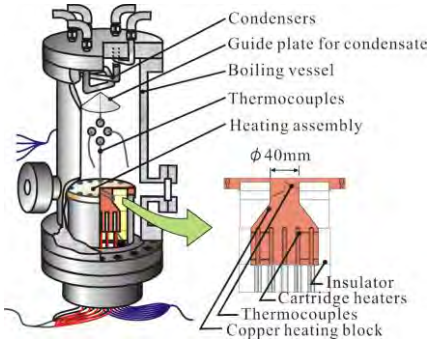

Fig.1 Experimental apparatus

The experimental apparatus is composed of a boiling vessel, condensers and a heating block assembly as shown in Fig.1. In the heating block assembly, the upper edge of the cylindrical copper block is operated as a heating surface which has a horizontal circular area with a diameter of 40mm facing upwards. The block is heated by the cartridge heaters inserted in the bottom. The design of the heating block is changed to increase the power of heaters corresponding to a heat flux of 4.5×10^6 W/m^2. In the block, thermocouples are inserted at different depths to evaluate the heat flux and the temperature on the heating surface. Heat transfer coefficients are evaluated by using the temperature of bulk liquid. The heat flux just before the value accompanied by the temperature excursion is regarded as CHF.

3. Characteristics of immiscible mixtures

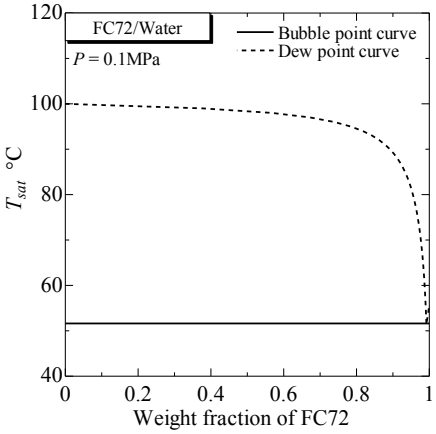

Fig.2 Phase equilibrium diagram

The vapor-phase and liquid-phase for each component are kept at the thermal equilibrium state under the system pressure, where the summation of saturated vapor pressures of the components at the equilibrium temperature becomes the total pressure. Figure 2 shows the phase equilibrium diagrams for FC72/Water at the total pressure of 0.1MPa. Higher saturated vapor pressure of more-volatile component compresses the less-volatile liquid above its saturation pressure corresponding to the equilibrium temperature, e.g. equilibrium temperature is 51.6°C, and higher subcooling 48.4K is given to the less-volatile liquid, water. On the other hand, the more-volatile liquid is compressed by the lower partial pressure of less-volatile component, and lower subcooling 4.3K is given to FC72. As a consequence, self-sustaining subcooling is given for immiscible liquids even under the pool boiling conditions.

4. Experimental results

4.1 Heat flux versus temperature difference and heating surface temperature

Figure 3 shows the relation between the heat flux q and

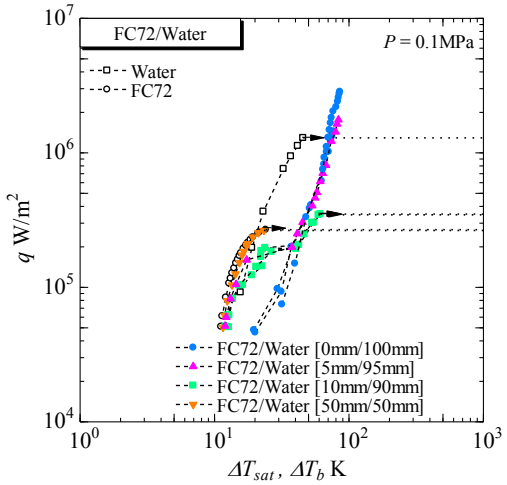

Fig.3 Boiling characteristics

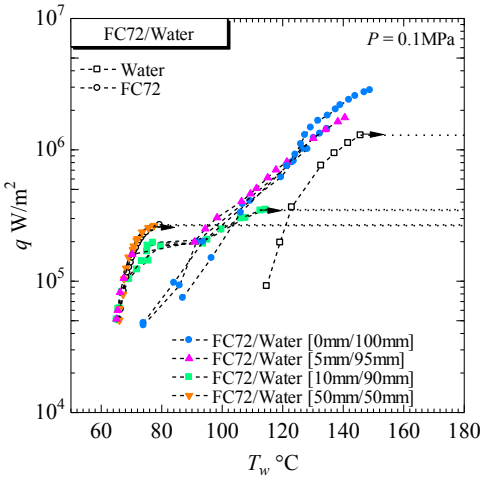

Fig.4 Heat flux versus heating surface temperature

temperature difference for FC72/Water. In the abscissa, the temperature difference ΔT_b between the heating surface and the equilibrium liquid temperature is used for the mixture at the subcooled state, while it is substituted by the surface superheat ΔT_{sat} for pure components at the saturation state under the same total pressure. In the case of small thickness for FC72 layer, i.e. FC72/Water [10mm/90mm] and [5mm/95mm], the local burnout and the small temperature excursion occur at the heat flux of around 2×10^5 [W/m^2] which is lower than that of pure FC72 and [50mm/50mm]. The reduction of CHF is deduced to be due to the shortage of FC72 supply for such small initial layer thicknesses. Authors named this temperature jump as "intermediate burnout". For a large thickness, i.e. FC72/water [50mm/50mm], the curve almost coincides with that for pure FC72 at the saturation state because of small subcooling of FC72 for the mixture. On the other hand, FC72 for [0mm/100mm] is filled only around the cylindrical heating block without the layer on the heating surface at least before the heating. The disturbance at the liquid-liquid interface around the cylindrical heating block is caused by the falling condensate droplets of more-volatile liquid with higher density in addition to the natural circulation in the vessel. As a consequence, a part of FC72 is carried on the heating surface, and the heat transfer characteristics at high heat flux become similar to those for [5mm/95mm]. Decreased heating surface temperature for FC72/Water [5mm/95mm] and [0mm/100mm] than pure water is observed by the aid of vaporized FC72 as shown in Fig.4.

4.2 Critical heat flux

The values of CHF accompanied by the surface temperature excursion are represented by the horizontal dotted lines in Figs. 3-4. The actual CHF values for the mixtures at FC72/Water [0mm/100mm] and [5mm/95mm] were not measured restricted by the available capacity of condensers. For FC72/Water [0mm/100mm], the maximum value of the heat flux measured becomes 2.85×10^6W/m^2, i.e. 2.2 times higher than CHF for pure water under the same pressure. The CHF value for FC72/water predicted by Ivey-Morris correlation [2] corresponding to the self-sustaining subcooling ΔT_{sub} =48.4K becomes as much as 4.3×10^6 W/m^2, far larger than the value for pure water. Such a drastic increase of CHF could be expected provided that the large layer thickness of more-volatile liquid does not disturb the change of liquid contacting the heating surface by intermediate burnout. The verification of larger CHF than obtained so far is scheduled by the improvement of cooling capacity of the boiling vessel.

5. Conclusions

Larger CHF values than that for pure water are obtained under the high subcooling condition resulted from the compression effect by the high vapor partial pressure of more volatile component. Moreover, in the less volatile dominated regime at the heat flux larger than that for intermediate burnout, the heating surface temperature is lower than that for pure less volatile component at the same total pressure. By these features, the boiling of immiscible mixtures has a great potential for the high-performance cooling systems for space or ground applications.

References

1) H. Kobayashi, N. Ohtani and H. Ohta: Proc. 9th International Conference on Heat Transfer, Fluid Mechanics and Thermodynamics, (2012) 771

2) H. J. Ivey and D. J. Morris: Proc. Third International Heat Transfer Conference, **3** (1966) 129

ISS における InGaSb 結晶成長実験に対する数値シミュレーション

○　ミルサンディ ハルヨ，山本卓也，高木洋平，岡野泰則（大阪大），稲富祐光（JAXA），
早川泰弘（静岡大）

Numerical Simulation of InGaSb Crystal Growth Experiment on the ISS

○　Haryo MIRSANDI, Takuya YAMAMOTO, Youhei TAKAGI, Yasunori OKANO (Osaka Univ.),
Yuko INATOMI (JAXA), Yasuhiro HAYAKAWA (Shizuoka Univ.)

1. Introduction

InGaSb ternary alloy semiconductor is a highly promising material for thermo-photo-voltaic devices. However, it is difficult to grow high quality homogeneous InGaSb crystals on Earth due to gravitational segregation occurring during growth. This adverse effect is minimized in the microgravity environment due to the absence of strong natural convection. InGaSb crystal growth experiments are being conducted using a GaSb/InSb/GaSb-sandwich system onboard the International Space Station (ISS) to investigate the effects of gravity and to understand interface kinetics during the growth process[1]. In the present study, the crystal growth process was numerically simulated in order to shed lights on the transport phenomena occurring in the solution of this sandwich system.

2. Numerical Method

The numerical model is two-dimensional and axisymmetric. The computational domain consists of the InGaSb solution, the GaSb solid crystals, and the crucible ampoule wall (**Fig. 1**). The governing equations in the liquid phase are the continuity, Navier-Stokes, energy, and diffusion equations. In the solid phases, the governing equation is the energy equation. The mass and heat balance equations are solved at the crystal/solution interface for considering the dissolution and growth of the crystal. Numerical simulations were carried out under both 1 G and microgravity level of 10^{-4} G that corresponds to the average gravity level observed on the ISS for comparison. Two values of heating rate were used: 10 °C/s and 0.06 °C/s (Table 1).

Table 1 Numerical conditions

Label	Heating rate (°C/s)	Gravity level (G)
Case A-1	10	1
Case A-2	10	10^{-4}
Case B-1	0.06	1
Case B-2	0.06	10^{-4}

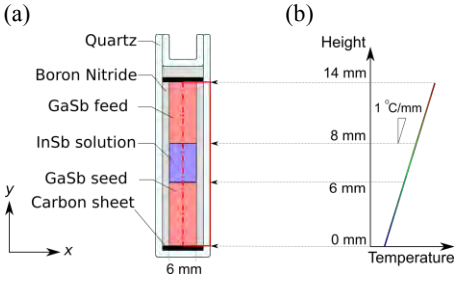

Fig. 1 (a) Ampoule configuration and (b) an ambient temperature profile.

3. Results and Discussion

Fig. 2 shows the time evolution of the center position of the seed/solution interface. The interface position of the seed/solution moved down first and then moved up slowly indicating that the crystal grew after the dissolution of GaSb seed crystal. In case of higher heating rate, at 3 min. of the process under 1 G, the solution reached supersaturation and the growth started. However, under 10^{-4} G, growth started at 5 min. It is because under 10^{-4} G, mixing in the solution became weak due to the suppression of solutal convection. Moreover, since convection enhances the upward transportation of GaSb solute near the seed/solution interface, the dissolution length of seed under 1 G was longer than that of under 10^{-4} G (**Fig. 3**). In case of lower heating rate, growth started almost at the same time and the dissolution lengths of seed crystals were almost the same under both gravity levels. This is due to the fact that in the case of lower heating rate, concentration gradient in the solution was low; as a result the solutal convection was suppressed even under 1 G conditions.

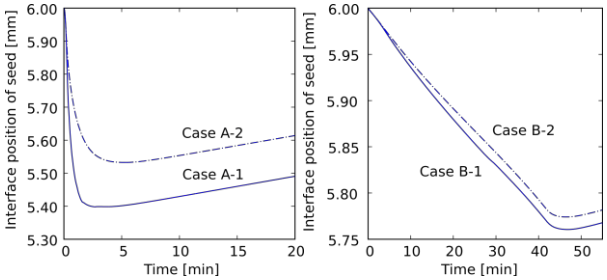

Fig. 2 Time evolution of the center position of the seed/solution interface.

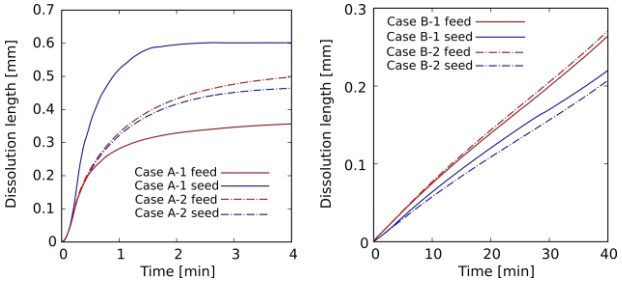

Fig. 3 Time evolution of dissolution length.

References

1)　M. Nobeoka, Y. Takagi, Y. Okano, Y. Hayakawa, and S. Dost: J. Crystal Growth, **385** (2014) 66.

超音波浮遊液滴の内外部流動と伝熱特性

○丹羽基能，合田篤（筑波大），長谷川浩司（工学院大），金川哲也，金子暁子，阿部豊（筑波大）

Flow Behavior and Heat Transfer Characteristics of an Ultrasonically Levitated Droplet

○Motonori NIWA, Atsushi GODA (Univ. of Tsukuba), Koji HASEGAWA (Kogakuin Univ.),
Tetsuya KANAGAWA, Akiko KANEKO, Yutaka ABE (Univ. of Tsukuba)

1. Introduction

The container-less processing using levitation techniques can prevent the heterogeneous nucleation and the contamination due to the container wall. It is expected to be used in analytical chemistry and production of new materials under microgravity environment. In addition, laser heating to a droplet is expected to be used in condensation of solution. An acoustic levitation is one of the levitation techniques, and induces the internal flow [1] and external flow which are dependent on volatility [2]. However, there are few experiments which evaluate the heat transfer performance of acoustically levitated droplets. This paper discusses the relationship between the heat transfer and flow characteristics of acoustically levitated droplets with evaporation and on laser heating.

2. Experiments

The experimental setup consists of a single axis acoustically levitator and measuring devices. The droplets are generated at the pressure node of the standing wave using a syringe. The size of droplets is millimeter-scale, and the shape of droplets is an ellipse. Three types of fluids are used: water, 50wt % aqueous solution of ethanol, and ethanol. The levitated droplet is visualized by a high speed camera in order to obtain velocity vector fields by PIV and observe the volume change. The temperature gradient near the surface and the surface temperature are measured by a thermocouple and an IR camera, respectively. In the case of heating, the upper part of a water droplet is heated by a 1.5 W YAG laser.

2.1 Internal and external flows of a levitated droplet

Fig. 1 (a) and (b) represent velocity vector fields of the internal and external flows of a non-heated water droplet, respectively. The internal flow rotates around the center of the droplet as a stagnation point (**Fig. 1 (a)**). On the other hand, the ambient air around a water droplet streams from both side regions toward the upper and lower regions. In addition, toroidal vortices are observed at the bottom of the droplet (**Fig. 1 (b)**).

2.2 Heat transfer characteristics of a levitated droplet

Fig. 2 (a) shows the heat transfer characteristics with evaporation. The heat transfer coefficient is estimated from the volume change and the temperature gradient near the droplet surface. From this result, the heat transfer of the acoustically levitated droplet is substantially higher than that estimated by the well-known empirical equations of a heat transfer characteristics around a sphere. It suggests that the complex external flow enhance the heat transfer characteristics.

Fig. 2 (b) shows the heat transfer characteristics on laser heating at the upper region of a water droplet. The heat transfer coefficients are calculated based on the volume change and temperature rise of droplets. We can confirm that Nusselt number, Nu, increases significantly. It is implied that the evaporation is induced intensively by laser heating and this enhances the heat transfer characteristics. Thus, the heat transfer characteristics on laser heating become more effective than that with evaporation.

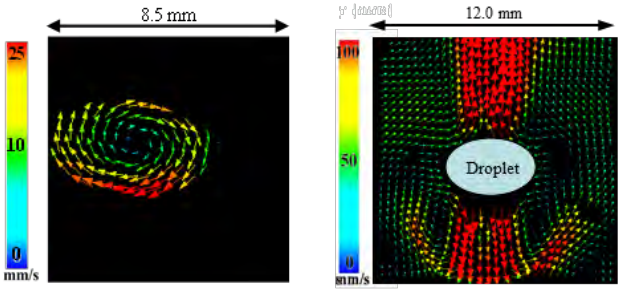

(a) Internal flow (b) External flow

Fig. 1 Internal and external flows of a water droplet

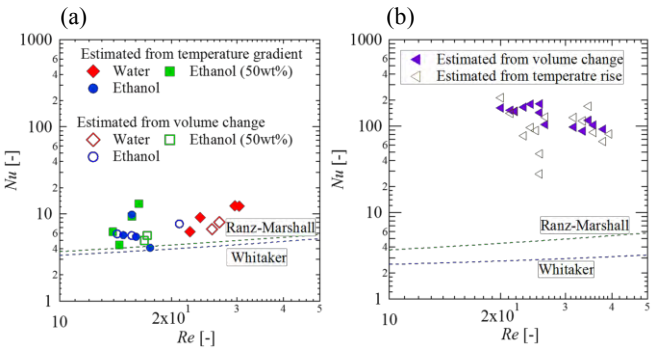

Fig. 2 Heat transfer characteristics of (a) droplets with evaporation and (b) water droplets on laser heating

References

1) Y. Yamamoto, Y. Abe, A. Fujiwara, K. Hasegawa and K. Aoki: Microgravity Sci. Technol., **20** (2008) 277.

2) K. Shitanishi, Y. Abe and A. Kaneko: Japanese J. Multiphase Flow, **26** (2013) 537.

P07

超音波浮遊液滴の界面近傍微小スケールにおける流動挙動と輸送現象

○合田篤（筑波大院），長谷川浩司（工学院大），金川哲也，金子暁子，阿部豊（筑波大）

Flow Behavior and Transport Phenomena in Vicinity of Interface around Ultrasonically Levitated Droplet

○Atsushi GODA(University of Tsukuba), Koji HASEGAWA (Kogakuin University), Tetsuya KANAGAWA, Akiko KANEKO, Yutaka ABE (University of Tsukuba)

1. Introduction

By using levitation techniques, the method called the container-less processing can remove influences of walls. An acoustic levitation is applicable to any objects. There are various practical studies: the separation of the mixed fluid by using evaporation behavior[1], and the contact-less mixing[2], and so on. On the other hand, an acoustically levitated droplet induces internal and external unsteady flows with nonlinearity. It is important to investigate the interaction of such a behavior and the phase-change process. Our group reported that the flow structure was different between with and without evaporation[3]. However, the cause of the flow generated around the levitated droplet with evaporation is unclear. In addition, it is important to understand heat transfer from the levitated droplet in actual application of the acoustic levitation method. The purpose of this study is to clarify the interaction between the flow behavior and transport phenomena around an acoustically levitated droplet. Hence, we measured the external flow, and volume and surface temperature of the levitated droplet, and evaluated the flow structure and heat transfer.

2 Results and discussions

Fig. 1 shows the visualization results of the external flow in the vicinity of droplet. In the case of water droplet, the surrounding fluid flows out to the upper and lower of the droplet. In contrast, in the case of the volatile droplet, the surrounding fluid flows from the upper and lower of the droplet. In addition, the circular vortices were observed in the vicinity of the volatile droplet. In addition, this result suggested that the size of circular vortex decrease with the increasing in the saturated vapor pressure.

To calculate the heat transfer coefficient from the time series change of the droplet volume, we assume that all the amount of heat given from the surrounding, are regarded as the latent heat of droplets. **Fig. 2** shows the result of heat transfer coefficient, and the curves denoted by estimated from Ranz-Marshal correlation[4]; the black solid curve represents the condition without the convection, and the red and blue dashed represent show the condition with the convection evaluated by the velocity in the vicinity of droplet. In the ethanol solution of 25 [wt%] and water, the circular vortex was not observed[5] and the heat transfer coefficient is the same value as Ranz-Marshall correlation. In the droplet with the circular vortex such as ethanol solution of 50, 75 and 100 [wt%][5], the heat transfer coefficient is larger than that estimated from Ranz-Marshal correlation. This result suggested that the heat transfer coefficient have been affected by the complex flow structure around the droplet.

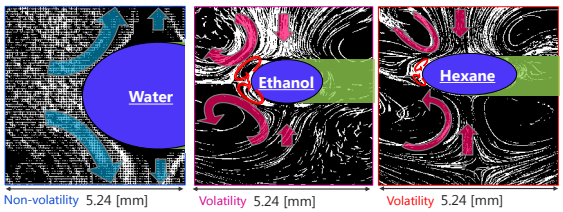

Fig. 1 The Flow trajectory of the external flow

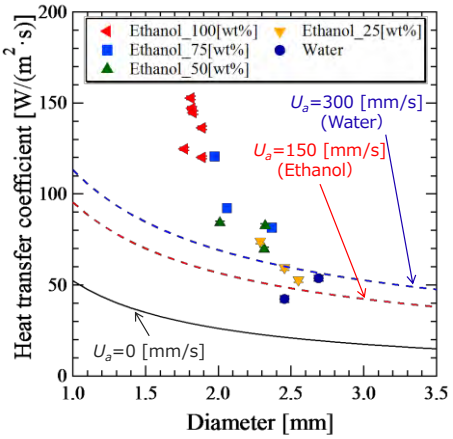

Fig. 2 Heat transfer coefficient of levitated droplet, where U_a is the velocity in the vicinity of droplet.

References

1) S. Santesson, I.B.R. Ramirez, P. Viberg, B. Jergil, and S. Nilsson: Analytical Chemistry, **76**, 2, 2004, 303.

2) D. Foresti, M. Nabavi, M. Kingauf, A. Ferrari, and D. Poulikakos: PNAS, **110**, 31, 2013, 12549.

3) H. Ishii, K. Hasegawa, A. Kaneko, and Y. Abe: Transactions of the Japan Society of Mechanical Engineers, Series B, **78**, 794, 2012, 1696.

4) W. Ranz and W. Marshall: Chem. Eng. Prog, **48**, 4, 1952, 141.

5) A. Goda, K. Hasegawa, A. Kaneko, and Y. Abe: Proc. Japan. Symp. Multiphase Flow, **A143**, 2014.

P08

航空機による微小重力環境を用いた金属液滴と溶融酸化物の濡れ性の観察

○小野寺健太，水野章敏，渡邉匡人（学習院大）

Observation of Wettability Between Melting Oxide and Liquid Metal Droplet under Microgravity Conditions by Parabolic Flight

○ Kenta ONODERA, Akitoshi MIZUNO, Masahito WATANABE (Gakushuin Univ.)

1. Introduction

The Oscillating drop technique with surface oscillation analysis is useful for measurements of thermophysical properties of high-temperature liquid by using the levitation technique. The conventional surface oscillation analysis derives surface tension and shear viscosity of liquid even on the ground conditions. Recently, modified surface oscillation analysis of compound droplets has been tried to measurement the interfacial tension of immiscible liquid system. However, modified surface oscillation analysis for compound droplets can be applied only in the microgravity conditions because the density difference separates two liquid parts under the ground. Interfacial tension is important thermophysical properties on the industrial process control, therefore, we propose the measurements of interfacial tension between steel melts and molten oxides using the electrostatic levitation furnace (ELF) in ISS with modified surface oscillation analysis. For preparation of ISS experiments, we performed parabolic flight experiments to confirm the formation of compound droplet, core-shell droplets, using liquid metals and molten oxides using the electromagnetic levitation method.

2. Droplet Dynamics

2.1 Simple droplet

The conventional surface oscillation technique is a suitable method for measurement of surface tension using noncontact technique. It assumes non-viscos droplet oscillates without external force. In this case, normal mode frequency ω_0 expresses surface tension σ_0 by Rayleigh's formula;

$$\omega_0{}^2 = \frac{8\sigma_0}{\rho_o R_o{}^3} \tag{1}$$

where ρ_o is density of droplet and R_o is radius of droplet. By replacement to $\rho_o R_o^3 = 3M/4\pi$, Eq.1 becomes the simple expression not to depend on the density. Under the gravity, it must correct the frequency by the expression of Cummings and Blackburn, it is because a sample transforms by gravitational influence and strong electromagnetic force. On the other hand, in microgravity condition, there is only one normal mode frequency of the simple droplet.

2.2 Two phases separated droplet

The normal mode frequency of the compound droplet, which is core-shell droplets by two phase separated liquids, must consider the interaction between core and shell by interfacial tension. In this system, two normal mode frequencies appear on the surface of shell liquid by following expression[3];

$$\omega_{\pm}{}^2 = K_{\pm}\frac{W}{J} \tag{2}$$

$$K_{\pm} = \frac{1}{2}\left(\frac{\sigma m_i}{\tau^3} + \frac{m_o\tau^3}{\sigma}\right) \pm \sqrt{\frac{1}{4}\left(\frac{\sigma m_i}{\tau^3} - \frac{m_o\tau^3}{\sigma}\right)^2 + 1} \tag{3}$$

$$\frac{W}{J} = \frac{\omega_0{}^2\tau^8}{\sigma}\frac{1}{(1+\Delta\rho_i)\tau^{10} + \frac{2}{3}\Delta\rho_i} \tag{4}$$

where

$$\begin{aligned} m_i &= \frac{3}{5}\tau^5 + \frac{2}{5}\tau^{-5} \\ m_o &= (1+\Delta\rho_i)\tau^5 - \Delta\rho_i\tau^{-5} \end{aligned} \tag{5}$$

$$\Delta\rho_i = \frac{3}{5}\frac{(\rho_i - \rho_o)}{\rho_o}\,. \tag{6}$$

In the eq.(2), $\omega_{\pm}$ are normal mode frequencies of the two phases separated droplet. $\sigma = \sqrt{\sigma_0/\sigma_{12}}$ and $\sqrt{R_o/R_i}$ is ratio of surface tension σ_0 and interfacial tension σ_{12}, ratio of radius, respectively. If we obtain $\omega_{\pm}$, we know the interfacial tension.

3. Experiment

For the observation normal mode frequencies of compound droplet, we developed a small electromagnetic levitation furnace (Parabolic Flight Experimental Facilities: PFLEX), which is able to put on board a airplane. The radio frequency current through the coils levitates the sample by Lorenz force. At the same time, it heats from joule heat, which caused by induction current at the sample surface. Using 2color-pyrometer and high speed recording system (250fps), we obtained droplet oscillation motion with its temperature. In order to melt oxide materials, we use the heat conduction from the liquid samples with Eddy current heating by RF current to the oxide samples. We used the starting samples of Ag partially covered with solid B_2O_3. Using the samples, we observed melting and wetting phenomena and surface oscillation of droplet from the top view by the parabolic flight during 20s.

4. Result and discussion

We success to observe wetting phenomena and surface oscillation for levitated droplet, which liquid Ag was covered with melted B_2O_3. Figure 1 (a) shows levitated droplet on the ground. On the ground conditions, liquid metal and molten oxide separates top and bottom like a snowman's shape. For the shape of liquid drop, we cannot apply to the formula of eq. (2)-(6). Figure1 (b) shows the observation results of liquid Ag covered by molten B_2O_3 under the microgravity condition.

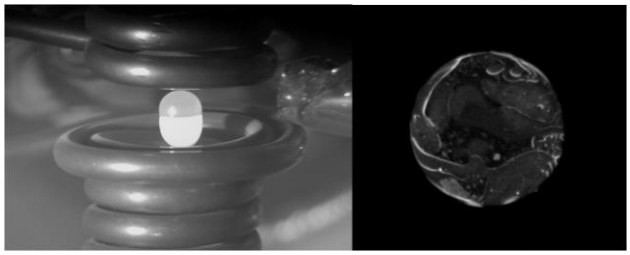

(a) (b)

Figure 1 (a)Side view of levitated sample on the ground and (b)top view of levitated sample under microgravity condition.

From the surface oscillation images of liquid Ag covered with molten B_2O_3 samples observed from the top view images, we obtained oscillation frequencies by FFT analysis. Figure2 shows power spectrum of FFT results, where Area is cross-sectional area of sample. According as R_x is sample radius of x-axis and R_y is its radius of y-axis, we define $R_+ = R_x + R_y$ and $R_- = R_x - R_y$, respectively. In the compound droplet oscillation, there are two peaks of normal mode frequencies, which considered the fully covered droplet model. However, in this experiment, the molten B2O3 fragmented without completely covering the Ag. The flow of B_2O_3 fragmented evoked Marangoni flow on the surface of the liquid Ag. Therefore, it is difficult to identify some peaks clearly. We discuss looking for a peak by appropriate mode choice carefully. The fragmentation phenomena of molten B_2O_3 would be cause by starting sample conditions. In this experiment, we used spherical Ag samples partially covered by solid B_2O_3. If molten oxide fully covers on liquid metal, we must prepare the samples, which solid oxide samples fully covers with the metal samples.

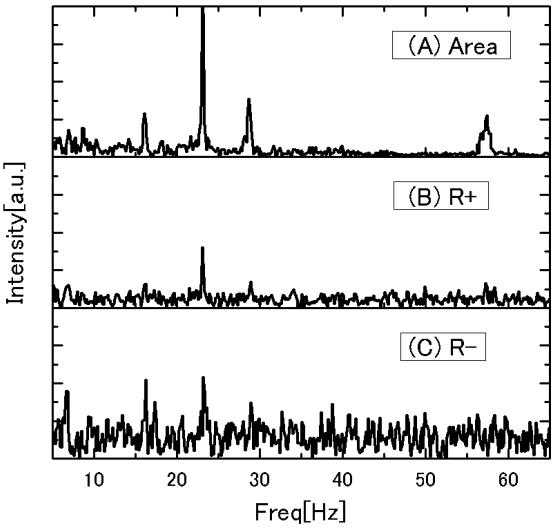

Figure 2 Comparative of oscillation frequencies of Ag+B2O3 droplet in microgravity condition.

6. Summary

We succeeded to levitate the compound sample which consists of Ag and B_2O_3 and to obtain surface oscillation frequencies. However, it is difficult to identify peak origins because in the present experiments liquid Ag sample partially covered by molten B_2O_3. For the future experiments, we prepare the starting metal samples fully covered by oxides to make compound droplets with core-shell structure.

References

1) L. Rayleigh: **29**, No.196-199, Proc. R. Soc. London(1879), pp.71-97.

2) D.L.Cummings and D.A.Blackburn: J. Fluid. Mech. (1991), **224**, pp.395-416

3) M.Saffren, D.D.Elleman and W.K.Rhim: Proc.2nd Int. Colloq. On Drop and Bubbles(1982), pp.7-14.

パラボリックフライトによる微小重力環境を利用した
柔軟宇宙構造物の軌道上挙動推定法

○丸木悠暉，嶋崎信吾，村田亮，宮崎康行（日本大学）

Estimation Method of Dynamic Behavior of Flexible Structure in Space Using Microgravity Environment by Parabolic Flight

○Yuki MARUKI, Shingo SHIMAZAKI , Ryo MURATA , Yasuyuki MIYAZAKI（Nihon University）

1. Background and Objectives

In recent years, the research on flexible large space structure is rapidly advanced in many country. Nihon university has launched a nano-satellite named "SPROUT" which demonstrates a concept of a flexible space structure. The main mission of SPROUT is deployment of a triangular membrane combined with inflatable tubes. In order to utilize the results of the on-orbit demonstration for the realization of flexible large space structure, it is important to predict the deployment motion in advance on the ground. There are several prediction methods, e.g. numerical simulation [1)2)3)] and experiment by using the small conceptual model [4)]. In this paper, the author proposes a new prediction method by the combination of 1G experiment and the microgravity experiment with ambient.

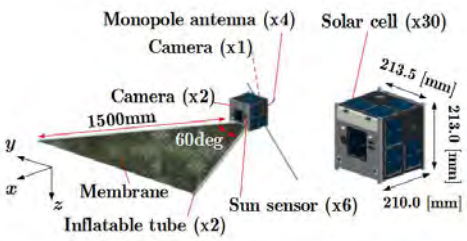

Fig. 1　Nano-satellite named "SPROUT"

2. Experimental Method

Fig. 2,3 show experiment sample and frame. Combined membrane is a triangle with each side about 440 mm. Inflatable tubes is extended by air with 70 kPaG.

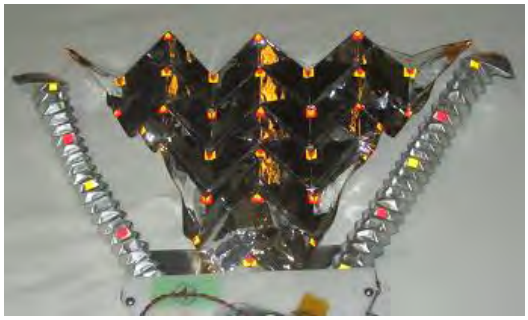

Fig. 2　Sample（combined membrane）

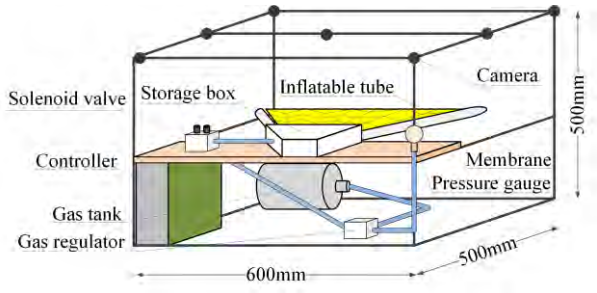

Fig. 3　Experiment frame

Dynamic behavior is recorded by some angle cameras and position of the three-dimensional coordinates is measured by stereovision from many markers on combined membrane.

3. Estimation Method and Results

Fig. 4 shows Definition of axis.

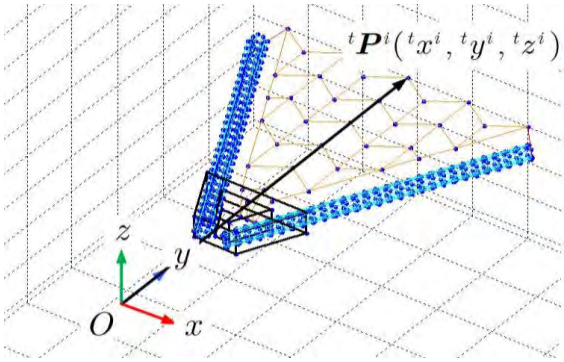

Fig. 4　Definition of axis and position vector

In this estimation method, it is assumed that the air density and the displacement is proportional. X and y axis displacement “d” on estimation is defined by the equation

$$\begin{cases} {}^t_x d_o^i = -\dfrac{{}^t_x d_g^i - {}^t_x d_\mu^i}{\rho_g - \rho_\mu}\rho_\mu + {}^t_x d_\mu^i \\ {}^t_y d_o^i = -\dfrac{{}^t_y d_g^i - {}^t_y d_\mu^i}{\rho_g - \rho_\mu}\rho_\mu + {}^t_y d_\mu^i \end{cases} \tag{1}$$

where ρ is the air density, subscript of upper left is time, upper right is number of node on combined membrane, left lower is

axial direction, and right lower is environment: o is estimation on orbit, g is 1G experiment, μ is microgravity experiment.

As well, influence of the air density and gravity about z axis displacement is corrected by the following equation

$$\begin{cases} {}_z^t d_\mu^{i\prime} = -\dfrac{{}_z^t d_g^i - {}_z^t d_\mu^i}{\rho_g - \rho_\mu}\rho_\mu + {}_z^t d_\mu^i \\ {}_z^t d_\mu^{i\prime\prime} = -\dfrac{{}_z^t d_g^i - {}_z^t d_\mu^i}{g_g - g_\mu} g_\mu + {}_z^t d_\mu^{i\prime} \end{cases} \quad (2)$$

where g is gravity acceleration. Furthermore, factor of proportionality k is expressed by the following equation.

$${}^t k = \frac{{}_y^t d_o^i}{{}_y^t d_\mu^i} = \frac{{}^{t+\Delta t} y_o^i - {}^t y_o^i}{{}^{t+\Delta t} y_\mu^i - {}^t y_\mu^i} \quad (3)$$

Z axis displacement on estimation is expressed by the following equation.

$${}_z^t d_o^i = {}^t k \cdot {}_z^t d_\mu^{i\prime\prime} \quad (4)$$

Fig.5 shows estimation of dynamic behavior on orbit by results of 1G experiment and microgravity experiment. **Fig.6** shows time history displacement of the node of the tip of the membrane. **Fig.7** shows the experiment condition in microgravity experiment: atmospheric pressure in the experiment plane, microgravity signal (Trigger), and acceleration of each axis.

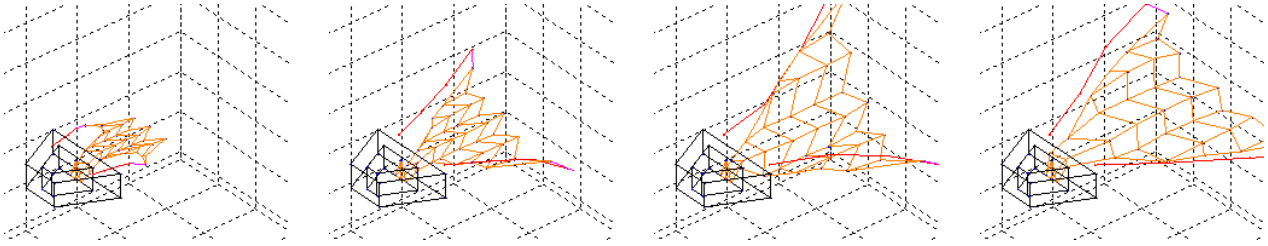

2.30 [sec] 4.40 [sec] 6.50 [sec] 8.60 [sec]

Fig.5 Results of estimation on orbit

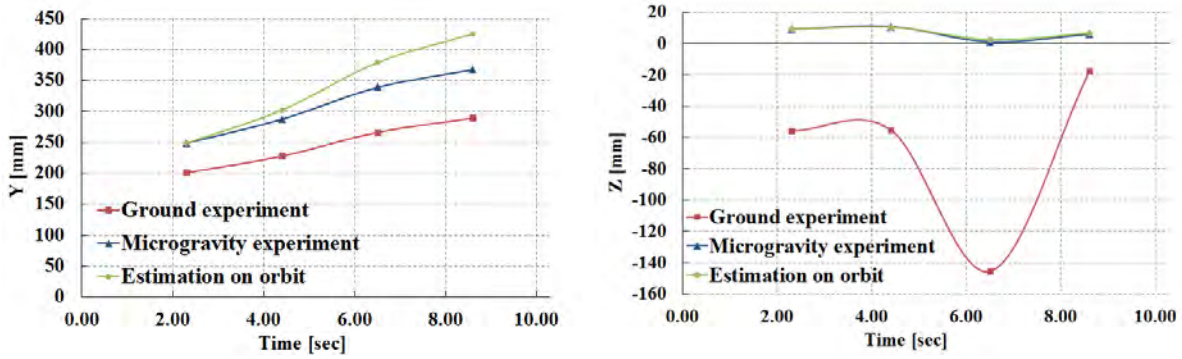

Fig. 6 Displacement of y axis direction (left) and z axis direction (right)

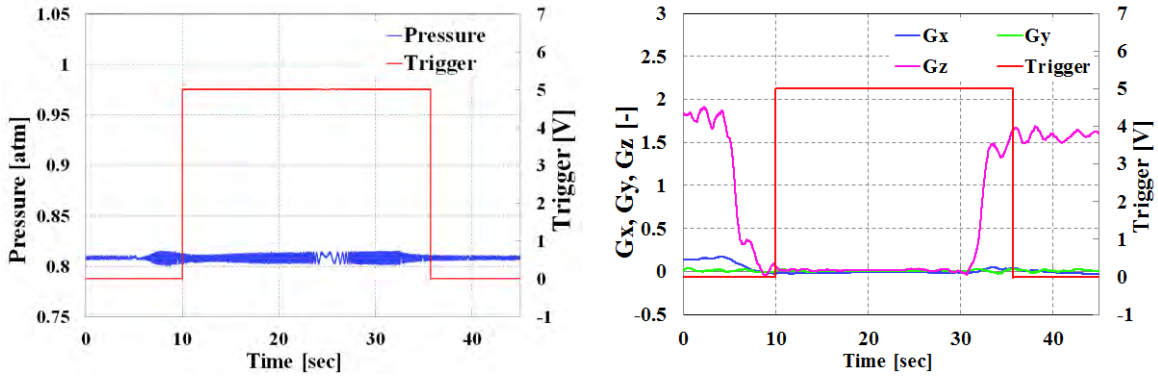

Fig. 7 Atmospheric pressure in plane(left) and gravity level(right)

From results of **Fig.6**(left)**,7**(left)**,** displacement of 1G experiment is 0.7～0.9 times smaller than that of microgravity experiment on y axis. And atmospheric pressure in microgravity experiment plane is about 0.8 times smaller than that in the 1Gexperiment. So assumption that the air density and the displacement is proportional has a validity.

From results of **Fig.6**(right)**,7**(right)**,** acceleration of each axis of microgravity experiment is about 0 G, and displacement of z axial direction of estimation and microgravity experiment is approximately equal. Therefore result of estimation of z axial direction has a validity.

4. Summary

Author experimented about deployment of combine membrane in 1G environment and microgravity environment. Also author estimated dynamic behavior on orbit by the combination of 1G experiment and the microgravity experiment.

In the future, we will conduct 1 G vacuum experiment, and estimate by result of that. Also we will study the similarity parameters, then, apply them to actual size combined membrane. By comparing the estimation and results on orbit by SPROUT, we will study a validity and accuracy of estimation.

References

1) A. Muta, S. Matsunaga and N. Okuizumi : 52nd The lecture meeting about strength of structure, Tottori, JSASS, 2010-3015, 2010.

2) M. Miyazaki, Y. Shirasawa, O. Mori, H. Sawada, et.al., Proc. 52nd SDM, AIAA , 2011-2181, 2011.

3) M. Yamazaki, A Study on Model Order Reduction for Nonlinear Structural Dynamics of Membrane Space Structure, 2011.

4) M. Yanagisawa : Similarity Rules for Spin-Deployable membrane, 2006.

物理学教育で使用できる無重力下ルーブ・ゴールドバーグマシンの作製

○窪田美紀（東京学芸大学大学院），岡本優輝，柿本嵩人，柳瀬綾花，吉永恭平（東京学芸大学）

Rube Goldberg Machines under Zero-Gravity that can be used in Physics Education

○Miki KUBOTA, Yuki OKAMOTO, Takahito KAKIMOTO,
Ayaka YANASE, Kyohei YOSHINAGA (Tokyo Gakugei Univ.)

1. Introduction

Many students have misconceptions in physics. Also many students feel that “Physics is difficult.” To motivate students in learning physics, we have developed a Rube Goldberg machine that shows several simple physics experiments. We ran this machine under micro-gravity, recorded this machine motion with video camera, and tested its educational effectiveness.

2. Equipment

We developed a Rube Goldberg machine that shows three experiments in physics. Experiments chosen for this machine were the motion of pendulum, relations of mass and acceleration, uniform linear motion. We named the section which showed the motion of pendulum as section A, relations of mass and acceleration as section B, uniform linear motion as section C. Details of each experiment is described. (Shown in Fig.1)

2.1 Section A

In the section A, we observed the motion of pendulum during 1g, 2g, and μg. The pendulums were started at 1g, and is observed during the machine goes through 2g and μg.

2.2 Section B

The section B is responsible for showing relations of mass and weight. Four arms with different weights are placed so that mass gradually grows larger. Constant elastic force is given to those weights. When the stopper is taken off, the observer can see the behavior of four arms. (Shown in Fig.2)

2.3 Section C

In the section C, we observed uniform linear motion on the rail using two iron balls. Two iron balls are equal in mass and size. These balls are hit at the same time with a lever, and they start to roll on the rails. There are magnets at the each end of the rails, and due to iron balls sticking to the magnets, electric circuits made of LEDs and motor are completed, and these will mark the end of this Rube Goldberg machine.

3. Classroom practice

We recorded the behavior of this machine with five digital video cameras. After editing the data into one video file, we showed the video to Tokyo Gakugei university senior high school and Kunitachi Metropolitan high school students to see if the video motivated students to think about physics, or made them interested in physics. As a result, students eagerly discussed about the results, were surprised that these simple experiments showed unexpected actions under micro-gravity. Also many students answered that they were interested.

4. Conclusion

Our Rube Goldberg machine performed expected motion in microgravity, and we succeeded in video recording. High school students are interested in our equipment and video, so this machine is effective in motivating high school students to think about physics.

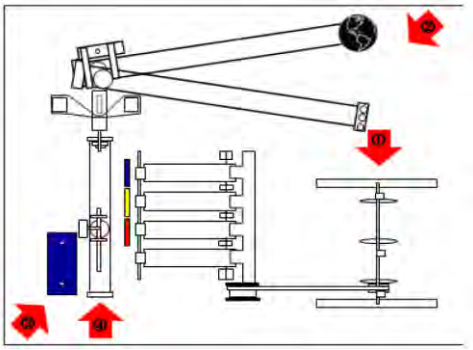

Fig.1 Overview of Rube Goldberg Machine
And camera settings
No.1 Section A recording
No.2 Section B recording
No.3 Section C recording
No.4 Section B/C connection recording

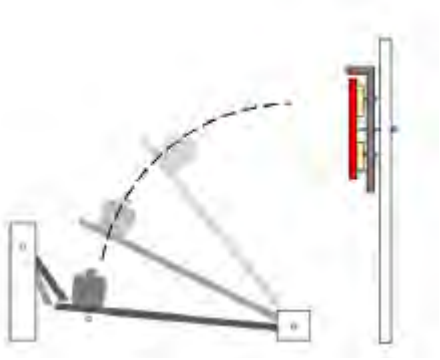

Fig.2 Schematic of Rube Goldberg Machine Section B

References

1) Masakazu KUNITOMO, Noboru TAKIGAWA, Kazuo MAKISHIMA, Toshiro KAWAMOTO, Tatehiko KURODA, Masanori KOBAYASHI, Teruo TAHARA, Michio HASHIMOTO, Tetsuo Masubuchi: High school physics, (2006) 166.

次世代宇宙用高機能ループヒートパイプの微小重力下での内部流動キャラクテリゼーション

○松田雄太，三富将敬，福嶋一貴，常新雨，長野方星（名古屋大）

Internal Flow Characterization of Next-generation Space Intelligent Loop Heat Pipe under Microgravity

○Yuta MATSUDA, Masataka MITOMI , Kazuki FUKUSHIMA, Xinyu CHANG, Hosei NAGANO (Nagoya Univ.)

1. Introduction

Loop heat pipes (LHP) are two phase heat transfer devices which utilize the capillary forces developed in porous media and latent heat at phase change of fluid. LHPs have been used for thermal control of spacecraft. However, more functional thermal control devices are required. A multiple evaporators LHP (MLHP) is one of the solutions. In order to predict its performance accurately, understanding of complex internal heat flow of the MLHP is required. In the past, observations of LHP under 1G are reported[1, 2]. Observation of LHP under μg is also reported[3]. However, there are no researches of visualizing internal flow of MLHP under μg. In this study, vapor-liquid distribution in the evaporator under μg is revealed.

2. Experiments

Fig. 1 shows the scheme of the MLHP for visualization. MLHP has two evaporators and compensation chambers (CCs). Insertion opening is provided to each CC to observe the inside by a bore scope. It is possible to observe both of the CC side and the wick core side by rotating the bore scope. The condenser is consisted by the transparent 1/8 inch tube made of PFA and the A15052 plate of 150×300mm. The condenser is cooled by conduction cooling with sandwiching the refrigerant and insulation between condenser plate and base plate. Measurement of the temperature distribution is carried out by 34 T-type thermocouples. The pressure is measured by 4 pressure gauges. Microgravity experiments were held at Diamond Air Service (DAS) in Komaki, Aichi. The available microgravity time by a parabolic flight is around 20s[3].

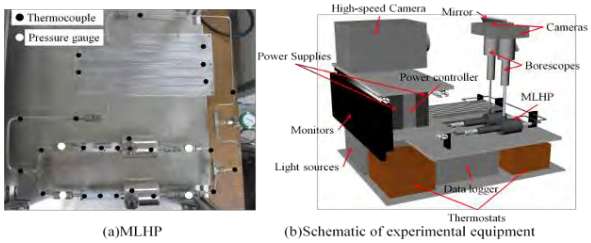

Fig. 1 Scheme of the MLHP

3. Result and Discussion

3.1 Vapor-liquid distribution in the evaporator and CC

Fig. 2 shows the internal observation of the evaporator of the heating side. Under 1g condition, the vapor phase is at the top of the core, and the liquid phase is at the bottom of the core (Fig. 2(a)). On the other hand, the vapor phase moves to the center of the core under μg. After that, the bubbles grow so as to extend to the CC side. Bubbles in the core never connect to bubbles of the CC (Fig. 2 (b), (c), (d)). Fig. 3 shows the internal observation of the CC of the heated side. The vapor phase is at the top of CC, the liquid phase is at the bottom of the CC under 1g (Fig. 3 (a)). Meanwhile the vapor phase moves in the center of the core as a large bubble (Fig. 3 (b)).

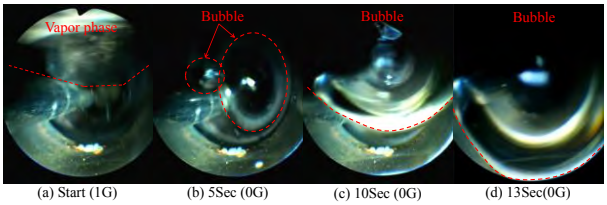

Fig.2 Inside of the evaporator (Heated side)

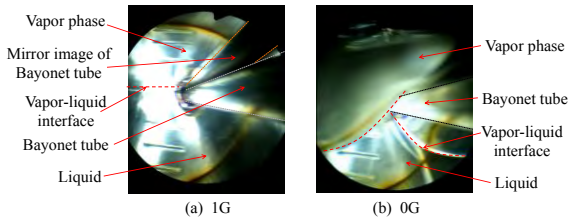

Fig. 3 inside of the CC (Heated side)

Fig. 4 shows the vapor-liquid distribution conceptual diagram of the heated evaporator and the CC. In the heating side, the vapor-liquid distribution follows gravity. The vapor phase is at the top of the CC, the liquid phase is at the bottom of the CC (Fig. 4 (a)). On the other hand, the effect of surface tension becomes dominant in μg. Because of this, the liquid stick to the wall and the bubbles gather in the center of the core.

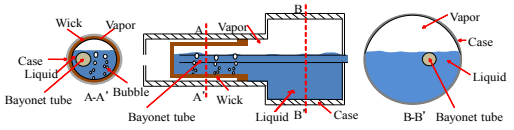

(a) Vapor-liquid Distribution Under 1g

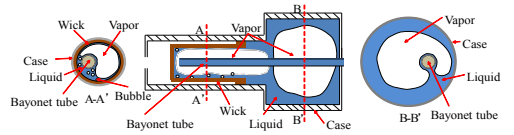

(b) Vapor-liquid Distribution Under μg

Fig. 4 Vapor-liquid distribution (Heated side)

References

1) B. P. d'Entremont, J. M. Ochterbeck, Proc. Of the ASME Summer Heat Transfer Conference, 2, 387 (2008)
2) J. M. Climbala, J. S. Brenizer, Po-Ya Chuang, S. Hanna, C. T. Conroy, D. R. Riley, Appl. Radiat. Isot, **61** (2004) 701-705
3) T. Ogushi, A. Yao, J. J. Xu, H. Masumoto, M. Kawaji, The Japan of Society of Mechanical Engineers, **66**,646 (2006) 230-235

パラボリックフライトによる微小重力曝露が換気効率ならびに自律神経活動に及ぼす影響

○平山佑介, 前沢寿亨, 田中雅侑, 傅秋光, 藤野英己(神戸大学)

Effects of Microgravity Induced by Parabolic Flight on Ventilation Efficiency and Autonomic Nervous Activity

○Yusuke HIRAYAMA, Toshiyuki MAEZAWA, Masayuki TANAKA, Akimitsu TSUTOU, Hidemi FUJINO
(Kobe University)

Abstract

Gravity plays a major role to determine respiratory function. For example, functional residual capacity (FRC) is reduced under microgravity condition [1-2]. The reduced FRC also decreases ventilation efficiency. However, it is not clear that acute effect of exposure to microgravity on ventilation efficiency. In addition, the relationship between ventilation efficiency and autonomic nervous activity during microgravity exposure has not been discussed. Therefore, we measured both ventilation efficiency and autonomic nervous activity, and discussed the changes under microgravity condition.

The data were divided into five phases by gravitational acceleration (Fig1A). Microgravity resulted in a reduction of the ventilation efficiency that was indicated by increase in minute ventilation-to-oxygen consumption ratio ($\dot{V}E/\dot{V}O_2$) and minute ventilation-to-carbon dioxide production ratio ($\dot{V}E/\dot{V}CO_2$) (**Fig. 1B, C**). In addition, the ratio of abdominal-to-thoracic motion (Vabd/Vrib) increased and the duration of expiratory phase of respiration (T_E/T_{Tot}) shortened during microgravity (**Fig. 1D, E**). Furthermore, LF/HF in sympathetic nervous activity was increased under microgravity (**Fig. 1F**). However, these results in Vabd/Vrib, T_E/T_{Tot}, and LF/HF were not consistent with previous reports [1, 3]. Finally, we observed using a video-recorder that subject's trunk was extended during microgravity exposure (**Fig. 2**).

It has been reported that abdominal motion becomes smaller as trunk is extended [4]. In addition, the decrease in the abdominal motion shortens expiratory time. Since prolonged expiratory had decreases sympathetic nervous activity [5], the decrease in the duration of expiratory phase might result in increasing sympathetic nervous activity during microgravity exposure. Therefore, the change of subject's posture could indirectly affect sympathetic nervous activity. These results suggest that autonomic nervous activity does not always play key role to regulate ventilation efficiency in case of exposure to microgravity.

Acknowledgement

This study was partly supported by the 11th student contest of microgravity experiments using an aircraft. We thank Japanese Aerospace Exploration Agency, Japanese Space Forum, and DIAMOND AIR SURVICE.

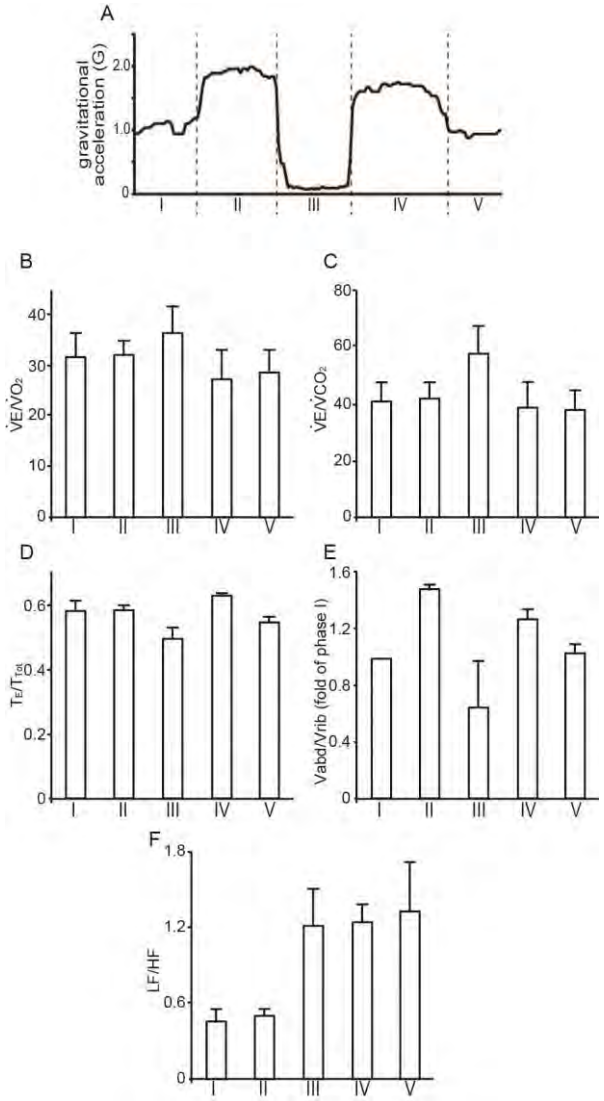

Fig. 1 Change of respiratory function and autonomic nervous activity

Fig. 2 Change of subject's posture during 1G and 0G

References

1) M. Paiva, M. Estenne, L. A. Engel: J Appl Physiol (1985), **67** (1989). 1542-50.
2) D. Bettinelli, C. Kays, O. Bailliart, A. Capderou, P. Techoueyres, J. L. Lachaud, P. Vaida, G. Miserocchi: J Appl Physiol (1985), **93** (2002). 2044-52.
3) B. Verheyden, F. Beckers, A. E. Aubert: Eur J Appl Physiol, **95** (2005). 557-68.
4) D. Paek, K. B. Kelly, F. D. McCool: J Appl Physiol (1985), **68** (1990). 2482-7.
5) T. Matsumoto, T. Masuda, K. Hotta, R. Shimizu, A. Ishii, T. Kutsuna, K. Yamamoto, M. Hara, N. Takahira, A. Matsunaga: Respir Physiol Neurobiol, **178** (2011). 275-82.

微小重力下における炊飯器内を想定した
三相系熱輸送の観察および地上実験との比較

○瀧本理仁，小林芳成，引地悠太（東京大）

Observation of Three-Phase Heat Transportation Simulating a Rice Cooker and Its Comparison between Microgravity and Ground Conditions

○Rihito TAKIMOTO, Yoshinari KOBAYASHI , Yuta HIKICHI (Univ. of Tokyo)

1. Introduction

The astronaut food and diet is one of the important problems in outer space. Taking food which are similar to what we usually take on earth is said to be effective to reduce stress in outer space. For us Japanese, eating freshly cooked rice in outer space is of great importance. Cooking rice contains physical phenomenon that rice is heated under gas-liquid-solid three-phase flow. Thermal convection caused by gravity play an important role when cooking rice on earth. However, under microgravity condition, heat convection does not occur because buoyancy caused by density difference does not exist. Therefore, there is a possibility of observation of other physical phenomenon dominating the thermal transportation. A large amount of study on heat transfer has been done including pool boiling and forced convective boiling using various microgravity facilities such as parabolic flight on airplanes, drop towers, and rockets, but no experiment has been done based on cooking in microgravity. In this study, the experimental vessels which contain water and rice is heated to boiling point in microgravity to obtain knowledge of the effect of microgravity condition on heat transportation of the liquid containing rice.

2. Experimental

The experiment was done during parabolic flight which enables to create microgravity condition below 3×10^{-2}G. The experimental apparatus is shown in Figure 1. The experimental apparatus consists of three parts including heating part, measuring part, and control part. It is difficult to cook rice from the beginning because duration of microgravity in this experiment is about 20s. Therefore, we used comparatively small vessel (ϕ 30mm×40mm) and measured the temperature history while heating to the boiling point. The surface temperature of the heater was kept to be 400℃ during ground condition, and 500 ℃ during microgravity using K-type thermocouple and heat regulator. The behavior of the boiling fluid in microgravity was recorded using video camera (SONY HDR-CX430V) and history of temperature inside the experimental vessel was recorded using data logger (OMRON ZR-RX70).

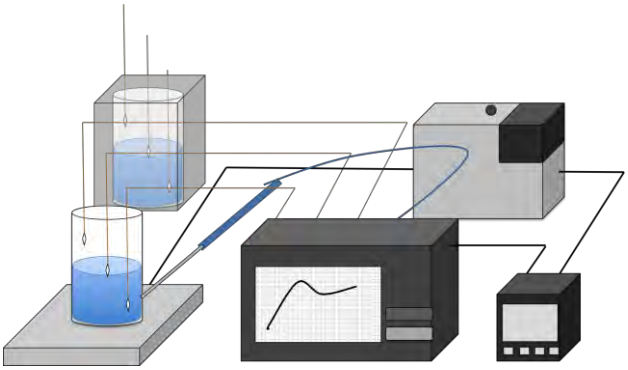

Fig.1 Schematic of Experimental Equipment

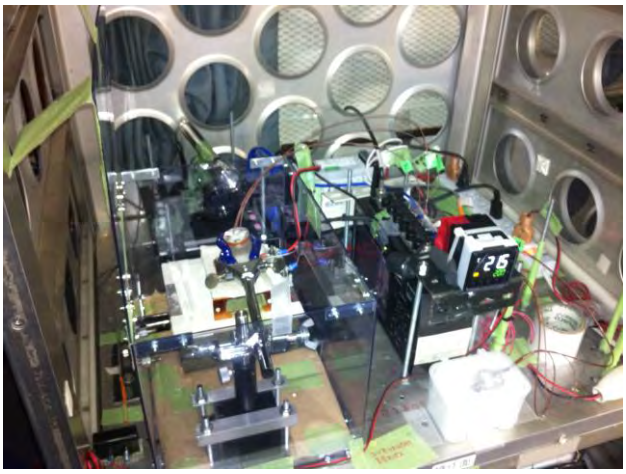

Fig.2 The overall view of the experimental equipment

3. Results and Discussion

The behavior of boiling fluid in microgravity is shown in Fig.3. The vessel of left figure contains 15cc of water and right vessel contains 30cc of water. The bubbles formed during microgravity didn`t coalesce and stayed individual. Bubbles formed from bottom surface that is closest to the heating part and the baby bubbles grew while pushing up older bubbles. During the development of bubbles, rice grains were observed to stir up. For the case of 15cc, the fluid stream up the wall of the vessel due to surface tension, and we predicted that this effect may enhance thermal transportation.

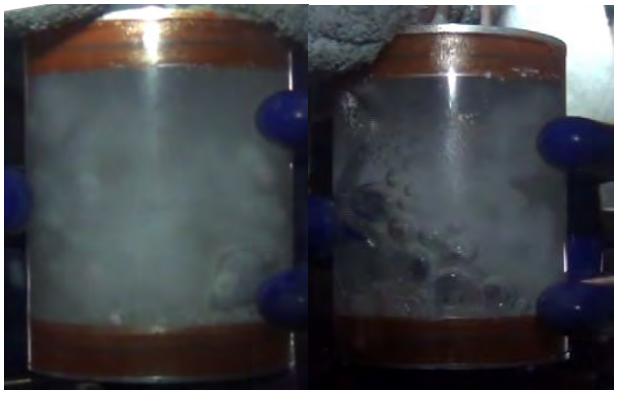

Fig.3 The behavior of the fluid while boiling in microgravity
(Left: 30cc of water, Right:15cc of water)

The comparison figure of heat transportation between microgravity and ground condition is shown in Fig.4-6. Temperature history was measured at 10mm, 20mm, and 30mm from the upper surface. For the case of Fig.4, the temperature in microgravity doesn't increase while it keeps increasing in 1g condition. This suggests that the thermal transportation is suppressed in microgravity. Fig.5 doesn't show clear difference between microgravity and ground, but from Fig.6, you can see that the temperature increases rapidly in microgravity condition compared to ground condition. Also, in 1g condition, the temperature seems to oscillate during heating. This may be due to convection caused by boiling.

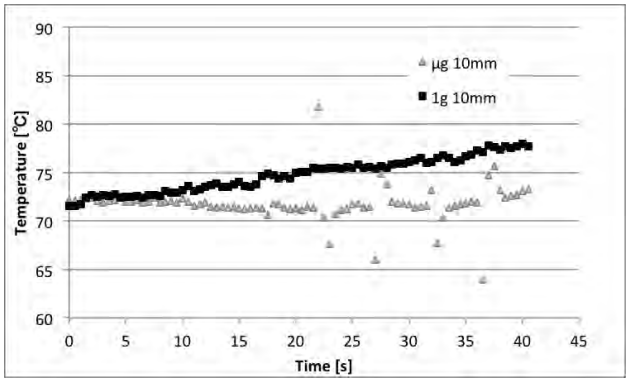

Fig.4 The hisory of temperature
(20mm from the upper surface of the experimental vessel)

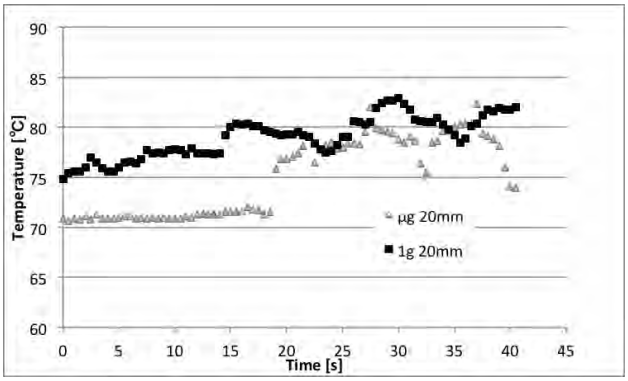

Fig.5 The hisory of temperature
(20mm from the upper surface of the experimental vessel)

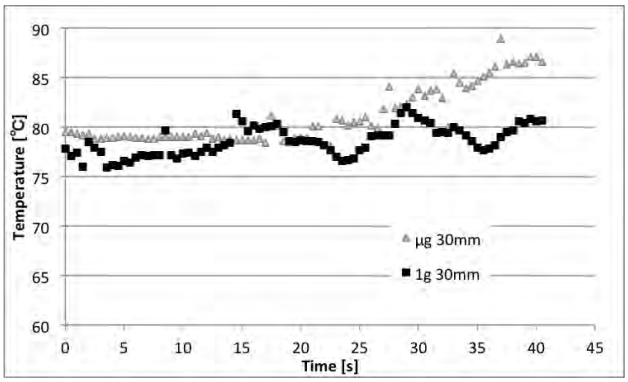

Fig.6 The hisory of temperature
(30mm from the upper surface of the experimental vessel)

4. Conclusion

1. Under microgravity condition, the boiling bubbles stayed individual.
2. The thermal transportation was suppresed in microgravity condition compared to ground condition.
3. Thermal concentration near heating surface was more significant under microgravity compared to ground condition.

References

1) NASA: Space food and nutrition An Educator's Guide with Activities in Science and Mathematics, 1999

2) A. F. Witt, H. C. Gatos, M. Lichtensteiger, M.C. Lavine and C. J. Herman: J. Electrochem. Soc., **122** (1975) 276.

3) K. W. Benz and G. Nagel: Proc. 5th Europ. Symp. Mat. Sci. under Microgravity, Schloss Elmau, FRG, Nov. 1984, 157

4) Johannes Straub; Boiling heat transfer and bubble dynamics in microgravity, Advances in Heat Transfer, **35** (2001) 57-172

微細流路内における非共沸混合媒体の強制流動沸騰熱伝達

○梅野晃太郎，岩田圭介，山崎優佑，大田治彦（九州大）

Flow Boiling Heat Transfer of Non-Azeotropic Binary Mixture in a Small-Diameter Tube

○Kotaro UMENO, Keisuke IWATA, Yusuke YAMASAKI and Haruhiko OHTA (Kyushu Univ.)

1. Introduction

In the thermal management system for space application, the development of the system which has no gravity effect is desired for reliable operation after ground tests. Flow boiling in mini tube is one of the promising means for cooling at high heat flux density because its interfacial behaviors and heat transfer are dominated by surface tension.

However, the flow fluctuation and partial dryout occur in flow boiling in mini tube because the vapor bubble grow towards also upstream and fill cross-section of the tube. As a consequence, no coherent experimental data was obtained so far, and it varies with different experimental manners and devices employed. To suppress flow fluctuation and to avoid the resulting partial dryout are essential requirement to clarify heat transfer characteristics in mini tubes.

We focus attention on the characteristics of non-azeotropic binary mixture such as alcohol aqueous solutions to reduce the vapor bubble growth rate by the mass transfer resistance existing inherently in the mixtures in order to suppress the flow fluctuation [1].

2. Experimental Apparatus

The outline of experimental apparatus is shown in **Fig.1**. The test section is a 0.51mm-diameter single mini-tube heated directly by the passage of alternative current. Nineteen thermocouples are soldered on the outer wall to evaluate the local heat transfer along the tube. The experimental conditions are summarized in **Table 1**. 1-Propanol/Water and 1-Butanol/Water are used as test fluids varying mass concentration under different combinations of mass velocity G and heat flux q.

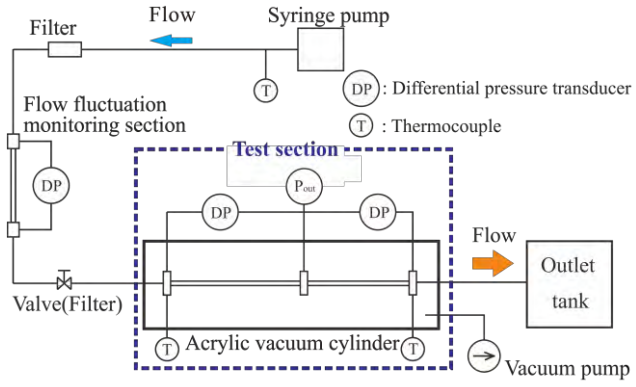

Fig.1 Experimental apparatus.

Table 1 Experimental conditions.

Tube inner diameter	d_i = 0.51mm	
Mass velocity	G = 100 – 200kg/m^{2}s	
Test fluid	1-Propanol/Water	2, 5, 10, 15, 20,72(Az.) wt% of 1-Propanol
	1-Butanol/Water	2, 4, 6, 7.15 wt% of 1-Butanol
Outlet pressure	P_{out} = 0.101MPa	
Heated length	L = 100mm	
Heat flux	q = 70 – 120 kW/m^2	

3. Experimental results

Saturated value of fluid temperature is evaluated from the liquid-vapor equilibrium diagram (**Fig.2**). Under saturated conditions, the increase of fluid temperature along the tube axis due to the preferential evaporation of more volatile component is calculated by the heat balance equation. **Fig.3** shows distribution of wall temperature T_w and fluid temperature T_f along the tube axis for 1-Propanol/Water (15wt% of 1-propanol) at G = 100kg/m^{2}s and q = 85kW/m^2. **Fig.4** shows the relation between heat transfer coefficient α and vapor quality x at different heat fluxes. **Fig.5 and 6** show the transition of pressure drop ΔP corresponding to the flow rate fluctuation in the heated tube and of wall temperature T_w at z = 35mm from the inlet of heated test section for pure water and 1-Propanol/Water (15wt% of 1-propanol). The results are summarized as follows.

1. At x = 0.06 - 0.1, heat transfer coefficient drop sharply because of the overshooting of wall temperature at the incipience of nucleate boiling.
2. Under the saturated condition of **Fig.3**, the wall temperature rises gradually which is consistent with the increased fluid temperature obtained from the calculation under the assumption of almost constant region.
3. In **Fig.4**, heat transfer coefficient decreases with increasing heat flux after the initiation of boiling. The trend is against the effect of heat flux on nucleate boiling heat transfer but is consistent with the effect of partial dryout which is emphasized at higher heat flux.
4. The use of single-component water or alcohol, a large flow fluctuation is observed, while it is drastically suppressed by using aqueous solutions (**Fig.5 and 6**). The result is along the objective of the present study.

4. Concluding remarks

The use of non-azeotropic mixtures seems to become a key technology to stabilize flow boiling in mini tubes in the application to the cooling of electronic devices with high heat flux density. However, it is well known that the heat transfer coefficient due to nucleate boiling of non-azeotropic mixture deteriorates from that of the single component liquid with the same thermal properties as the relevant mixture or from the interpolated value of heat transfer coefficient between those of single components. Further investigation is needed to evaluate the heat transfer characteristics for mixtures in flow boiling of mixtures in the entire quality range.

5. References

1) J.R. Thome and R.A.W. shock, "Boiling of Multicomponent Liquid Mixtures", *Advances in Heat Transfer*, Academic Press, Vol.16, 1984, pp. 59-156.

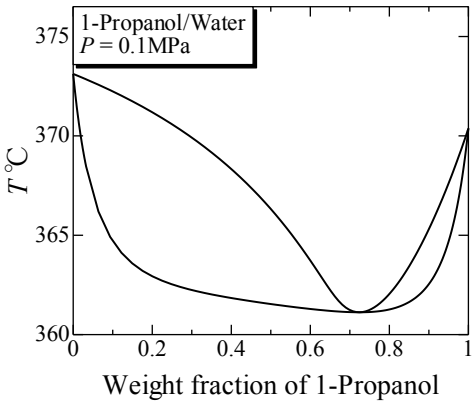

Fig.2 liquid-vapor equilibrium diagram.

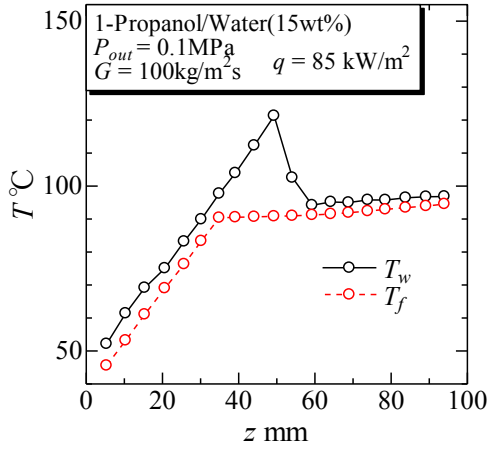

Fig. 3 Distribution of wall temperature T_w and fluid temperature T_f.

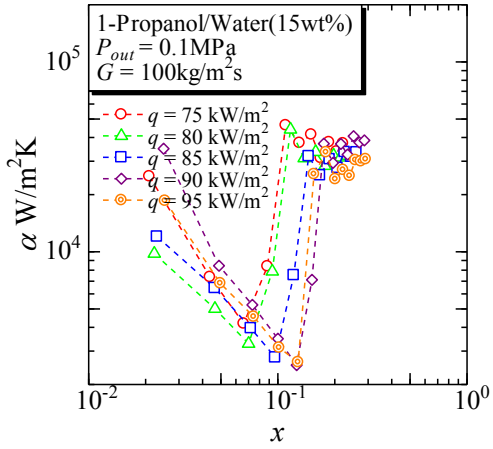

Fig. 4 Heat transfer coefficient α versus vapor quality x.

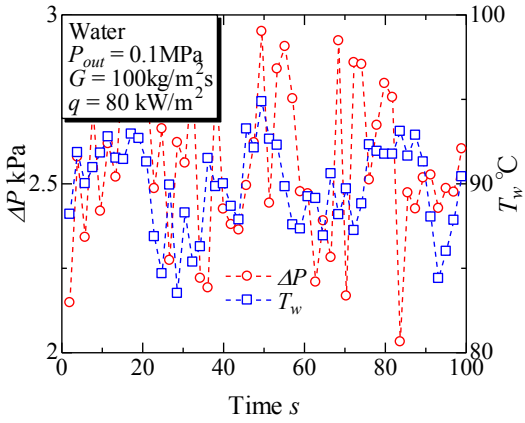

Fig. 5 Fluctuation of flow rate represented by the pressure drop ΔP and of wall temperature T_w at z = 35mm for pure water.

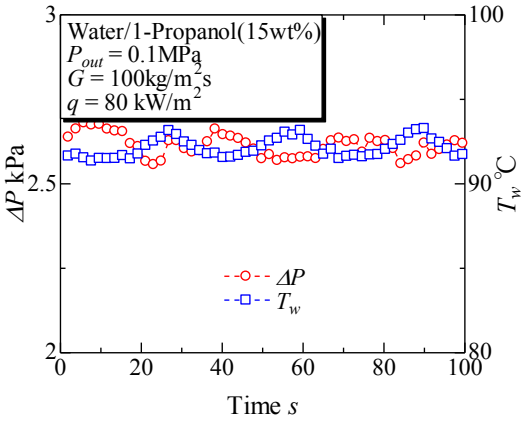

Fig. 6 Fluctuation of flow rate represented by the pressure drop ΔP and of wall temperature T_w at z = 35mm for 1-Propanol/Water (15wt% of 1-propanol).

一成分二相流のボイド率特性に及ぼす管径の影響

○五明泰作，浅野等（神戸大学）

Effect of Tube Diameter on Void Fraction Characteristics of One-Component Gas-Liquid Two-Phase Flow

○Taisaku GOMYO, Hitoshi ASANO (Kobe Univ.)

1. Introduction

Two-phase flow loop system has been attracting attention as a cooling and temperature control system for space structure. For the design of this system used in space, it is important to clarify the two-phase flow dynamics under microgravity. In a reduced gravity condition, the effect of surface tension on two-phase flow behaviors becomes larger. On the other hand, the effect also becomes larger with decreasing the channel diameter. In this paper, the transition of dominant force, especially between gravity and surface tension, and gravity and inertia force, was discussed based on void fraction characteristics. Void fraction was measured by a capacitance method.

2. Experimental setup

Vertical upward two-phase flows were examined for 2.0 and 4.0 mm diameter tubes. FC-72 was used as the refrigerant. The refrigerant was circulated by a gear pump. The inlet conditions were maintained by heat input at a pre-heater and a main heater, and then two-phase flow was supplied to the vertical observation section with the configuration as shown in **Fig. 1**[(1)]. In the observation section, void fraction measurement by a capacitance sensor and flow behavior observation by a high speed camera were conducted simultaneously. The detail of the measurement was reported in the previous report (1).

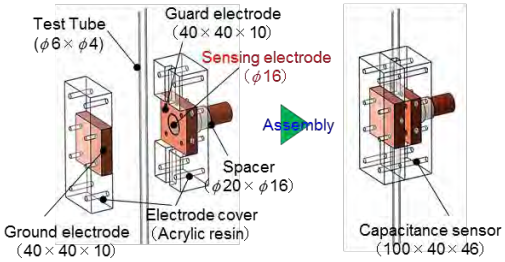

Fig. 1 Capacitance sensor for void fraction measurement.

3. Experimental results

Flow patterns observed in the test section were classified into bubble flow, slug flow, churn flow, semi-annular flow, and annular flow for each tube diameter. Churn flow was defined as the flow with intermittent liquid reverse flows. The flow pattern maps for 4.0 and 2.0 mm tubes with the Mishima-Ishii's transition boundaries[(2)] are shown in **Fig.2(a), (b)**, respectively. The flow pattern transition boundaries agreed well with the Mishima-Ishii's transition boundaries when semi-annular flow was included in slug flow.

Average void fractions for annular flow were arranged based on drift-flux model, as shown in **Fig. 3(a), (b)**. For 4.0 mm, average void fraction measured by capacitance sensor, α_{ave}, agreed well with the Ishii's annular flow model[(3)]. However, for 2.0 mm, the Ishii's model over-estimates a little. The reason might be on the flow behaviors. Void fraction at lower j_L might be lower due to higher liquid velosity with large waves.

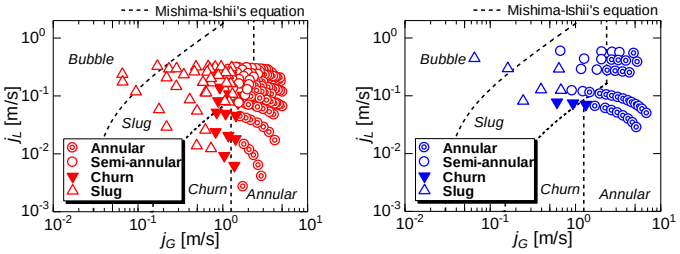

(a) D_{in} = 4.0 mm. **(b)** D_{in} = 2.0 mm.

Fig. 2 Flow pattern map with Mishima-Ishii's transition boundaries[(2)].

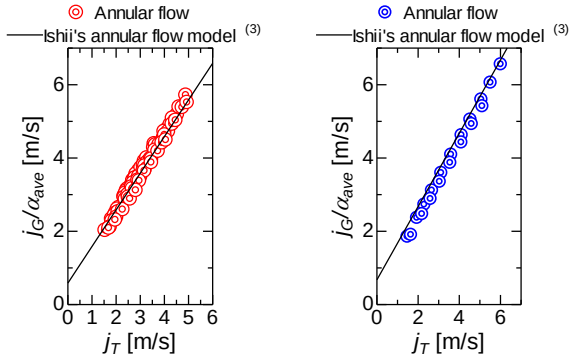

(a) D_{in} = 4.0 mm. **(b)** D_{in} = 2.0 mm.

Fig. 3 Average void fractions arranged based on the drift-flux model.

References

1) T. Gomyo, H. Asano, H, Ohta, Y. Shinmoto, O. Kawanami, T. Kurimoto, M. Komasaki, A. Matsumoto, Japanese Journal of Muntiphase Flow, **27**, 5, 2014, 547-554

2) K. Mishima, M. Ishii, Int. J. Heat Mass Transfer, **27**, 1984, 723-737

3) M. Ishii, ANL Report, ANL-**77-47**, 1977

ガスジェット浮遊法を用いた C12A7 エレクトライドの作成における酸素分圧の影響

○松原宏次，水野章敏，渡邉匡人（学習院大）

Effect of Oxygen Partial Pressure on Preparation of C12A7 Electride by using Conical Nozzle Levitation

○Koji MATSUBARA, Akitoshi MIZUNO, Masahito WATANABE

(Department of Physics, Gakushuin University)

1. Introduction

The compound $12CaO\text{-}7Al_2O_3$ (C12A7) is well known as an insulator used for cement raw materials. However, it was recently discovered that the compound became the conductive material called the electride by replacing an oxygen ion loosely bound in the cage structure with an electron.[1] The C12A7 electride can be prepared by extracting an oxygen ion in the cage structure under the reducing atmosphere. In addition, the vitrification of the C12A7 electride has been also reported.[2] In this case, it is necessary to use a quenching method to vitrify the C12A7 melt. Therefore, we made an attempt to prepare the C12A7 electride glass by using the conical nozzle levitation (CNL) technique which is known as a method to suppress a nucleation in a melt efficiently. In this study, we investigated an influence of the oxygen partial pressure on solidification of the C12A7 melt under different gas environments around the sample.

2. Experiment

Figure 1 shows the schematic illustration of the CNL apparatus. A spherical sample of C12A7 compound about 2 mm in diameter was prepared from a powder of CaO and Al_2O_3 by melting with the use of a CO_2 laser. Containerless solidification of the C12A7 compound was conducted under different gas environments. We used three kinds of gas, air ($PO_2=2\times10^4$ Pa), Ar ($PO_2=10$ Pa) and $Ar/H_2(7\%)$ ($PO_2=10^{-19}$ Pa), which have different oxygen partial pressure. In addition, we investigated a influence of the sample temperature, heating time and internal pressure in the chamber.

3. Results and discussion

Figure 2 shows the C12A7 samples solidified under the different gas atmospheres. Conventional XRD measurements confirmed that the samples vitrified. It was found that the sample became transparent when solidified in the air or the Ar atmospheres. On the other hand, when solidified in the $Ar/H_2(7\%)$ atmosphere, the color of sample showed dark green. The dark green coloring of C12A7 sample was reported as a peculiar feature of C12A7 electride. [1] This indicates that the reducing condition due to the $Ar/H_2(7\%)$ gas promoted a substitution of an oxygen ion in the cage to an electron. By increasing the internal pressure in the chamber from 1 atm to 1.5 atm, the coloring of sample in the $Ar/H_2(7\%)$ atmosphere was pronounced. Furthermore, when keeping the melt at 2073 K before cooling, the coloring of sample in the $Ar/H_2(7\%)$ atmosphere was promoted than keeping it at 2273 K. Meanwhile, a distinct difference was not observed by changing the keeping time of the melt.

In this talk, we will discuss an effect of oxygen partial pressure on preparation of C12A7 electride by using conical nozzle levitation.

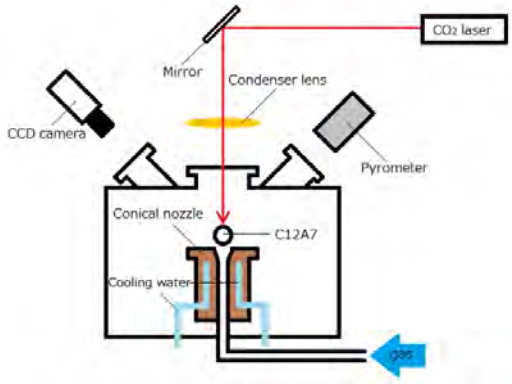

Fig.1 Schematic illustration of experimental set up using the conical nozzle levitation apparatus.

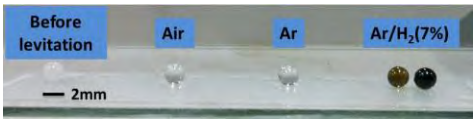

Fig.2 The C12A7 samples solidified by using conical nozzle levitation under different gas atmospheres.

References

1) S. Matsuishi et al., Science, **301**, (2003) 626
2) S. W. Kim et al., Science, **333**, (2011) 71

過冷メルトからの急速凝固における Double Recalescence

○加藤寛隆，永山勝久（芝浦工大），稲富裕光，M. S. Vijaya KUMAR，栗林一彦（ISAS/JAXA）

Double Recalescence during Rapid Solidification into Undercooled Melt

○Hirotaka KATO, Katsuhisa NAGAYAMA, Yuko INATOMI, M. S. Vijaya KUMAR
and Kazuhiko KURIBAYASHII

1. Introduction

On the thermodynamic criterion for forming a metastable phase from undercooled melt (*Mat. Sci. Eng. A*, **449-451** (2007) 675), we carried out the containerless solidification to verify the validity of the criterion using $LuFeO_3$ as the model material. In $LuFeO_3$, hexagonal modification (*h*-$LuFeO_3$) was formed as the metastable phase and the criterion was well satisfied. In $YbFeO_3$, however, X-ray diffraction shows the mixed structure of *h*-$LuFeO_3$ and *o*-$YbFeO_3$ (orthorhombic perovskite). This result suggests that *o*-$YbFeO_3$ also nucleated although the criterion for *h*-$LuFeO_3$ to nucleate is satisfied. In this study, in order to make clear the reason why the mixed structure is constituted in the sample of $YbFeO_3$, we observe precisely the solidification sequence using a high-speed video (HSV) and investigate the thermodynamic condition.

2. Experimental

As a tool for performing the sample to undercool, we used aero-dynamic levitator ADL. The spherical sample which is trapped inside the conical nozzle of ADL by the pressure difference of oxygen gas was melted completely by the irradiation of CO_2 laser beam from the top of the nozzle. The temperature of samples was measured with a mono-color pyrometer, whose sampling rate and the emissivity were fixed to 1 kHz and 0.8, respectively.

3. Results and Discussion

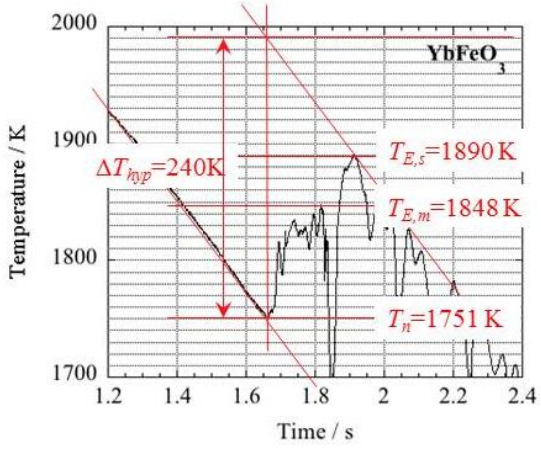

Fig. 1. Temperature-time relation of $YbFeO_3$

Figure 1 shows the typical *T*-*t* curves of $YbFeO_3$. In this figure, the curve after the recalescence is unsteady compared with that before the recalescence. This unsteadiness is owing to the unstable positioning of the sample in the conical nozzle because *h*-$YbFeO_3$ shaped a polyhedron similar to that of $LuFeO_3$. However, the peculiar point that is different from the curve of the $LuFeO_3$ sample is that the post-recalescence temperature shows two stages, corresponding to double recalescence. Post-recalescence temperature $T_{E,s}$, undercooling ΔT_s and hyper-cooling limit ΔT_{hyp}, which are required for analysis of the criterion, are 1848 K, 97 K and 240 K, respectively. The critical index calculated by using these values obviously satisfy the criterion. Nevertheless, mixed structure with *o*-$YbFeO_3$ was formed in the as-solidified sample. The first stages are approximately at 1850 K and the hyper-cooling limit at 1890 K, respectively.

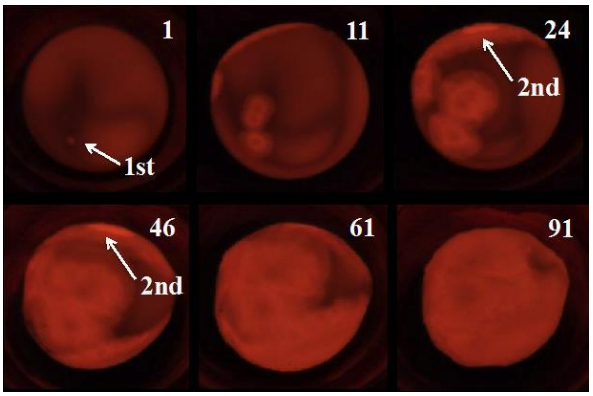

Fig. 2. HSV images of YbFeO3 captured during recalescence. The frames are taken at a time interval of 0.001 s, and the elapsed time indicated in each image was set to 0 s for one frame before the

Figure 2 shows the HSV-images captured during the recalescence. As time *t* passes from the onset of recalescence, the form of the sample changes to a polyhedral shape from spherical one. If the first recalescence corresponds to forming the metastable *h*-$YbFeO_3$, the *T*-*t* curve must satisfy the criterion for forming the metastable phase. In fact, the critical index, σ_c, is larger than 1.0; that means the criterion is satisfied. However, the second recalescence suggests the competition between growth of the metastable phase and the nucleation of the stable phase. Based on this suggestion, we regard this competition as

the decisive factor for double recalescence, and calculated the relative relation of the activation energies for forming a 2D nucleus of *h*-$LnFeO_3$ and a heterogeneous nucleus of *o*-$LnFeO_3$.

According to the neg-entropy model for the interfacial free-energy, the activation energies for forming a 2D nucleus ΔG^*_{2D} and a heterogeneous nucleus ΔG^*_{hetero} are respectively given by

$$\Delta G^*_{2D} = \frac{\pi h \alpha^2 \Delta S_f^{ms} T^2}{\left(N_A V_m^2\right)^{2/3} \Delta T^{ms}}, \quad (1)$$

$$\Delta G^*_{hetero} = \frac{16\pi \alpha^3 \Delta S_f^{s} T^3}{3 N_A V_m^2 \left(\Delta T^s\right)^2} f(\theta). \quad (2)$$

where N_A, V_m, ΔS_f, T, h, α, γ_l, and ΔG_V are Avogadro's number, molar volume, entropy of fusion, temperature, ledge height of 2D nucleus, interfacial free–energy and Gibbs free-energy difference, respectively. $f(\theta)$ that is acatalytic potency for heterogeneous nucleation, depends on the contact angle θ of a nucleus cap to a substrate and is given by

$$f(q) = \frac{1}{4}\left(2 - 3\cos q + \cos^3 q\right).$$

By using the relation $V_m = h^3 N_A$, the dimensionless forms of Eqs. 1 and 2 are expressed as follows:

$$\Delta G^*_{2D} = \frac{\pi C_p \Delta T_{hyp}^{ms} \overline{T}^2}{4 N_A \overline{T^{ms}} \left(\overline{T^{ms}} - \overline{T}\right)}, \quad (3)$$

$$\Delta G^*_{hetero} = \frac{2\pi C_p \Delta T_{hyp}^{s} \overline{T}^3}{3 N_A \left(1 - \overline{T}\right)^2} f(\theta), \quad (4)$$

where

$$\overline{\Delta T} = \frac{\Delta T^s}{T_E^s}, \quad \overline{T^{ms}} = \frac{T^{ms}}{T_E^s} \quad \text{and} \quad \overline{T} = \frac{T}{T_E^s}.$$

Figure 3 shows ΔG^*_{2D} and ΔG^*_{hetero} as a function of $\overline{T}$. In this figure, $\overline{T^{ms}}$ and $f(\theta)$ were used as parameters under the assumption that $\Delta T_{hyp}{}^{ms}$ is half of $\Delta T_{hyp}{}^{s}$: $\Delta G_{2D}{}^*$ was calculated for two cases: one is that $\overline{T^{ms}}$'s are 0.984, the other is 0.974; those are the dimensionless melting temperatures of *h*-$LuFeO_3$ and *h*-$YbFeO_3$, respectively. On the other hand, as for ΔG^*_{hetero}, three cases that $f(\theta)$'s are 0.01, 0.02, and 0.05 are calculated.

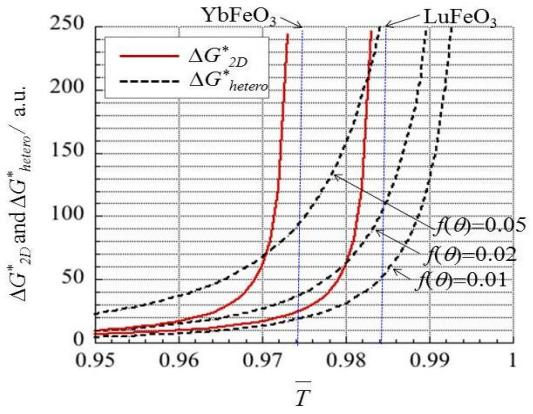

Fig. 3. Relation between $\Delta G_n{}^*$ for 2D homo-epitaxial nucleus of $\overline{T}$

Therefore, if the melt of $LuFeO_3$ is undercooled to the temperature $\overline{T} \le 0.98$, that is approximately 0.4 % lower than $T_E{}^{ms}$ of *h*-$LuFeO_3$, ΔG^*_{2D} of *h*-$LuFeO_3$ becomes smaller than ΔG^*_{hetero} of *o*-$LuFeO_3$, under the condition that $f(\theta)$ is 0.02, and, as a result, double recalescence does not occur. On the other hand, even if the criterion for forming a metastable phase is satisfied and $f(\theta)$ is 0.02, the double recalescence occurs and the mixed structure of *h*-$LnFeO_3$ and *o*-$LnFeO_3$ is formed in the as-solidified sample whose $\overline{T^{ms}}$ is less than 0.975, because in this sample $\Delta G_{2D}{}^*$ is absolutely larger than ΔG^*_{hetero}. $YbFeO_3$ is one of the cases of these materials.

4. Summary

In $YbFeO_3$, double recalescence that suggests the nucleation of orthorhombic perovskite was observed although the criterion for forming a metastable phase was satisfied. The analysis of the activation energies for forming a two dimensional nucleation of metastable phase and the heterogeneous nucleation of stable phase shows that double recalescence occurs if the difference of melting temperatures of stable phase and metastable phase is large and the undercooling is smaller than the critical ones. If compared the melting temperature of $YbFeO_3$ with that of $LuFeO_3$, the former is 1 % larger than the latter; This difference is sufficient for double recalescence to occur.

InGaSb 結晶成長に対する重力効果
―国際宇宙ステーション内の微小重力下と 1G 下実験―

○Velu NIRMAL KUMAR, Mukannan ARIVANANDHAN, Govindasamy RAJESH, 小山忠信, 百瀬与志美（静岡大）, 稲富裕光, 阪田薫穂, 石川毅彦, 高柳昌弘,上垣内茂樹（JAXA）, 小澤哲夫（静岡理工科大）, 岡野泰則（大阪大）, 早川泰弘（静岡大）

Effect of Gravity on InGaSb Crystal Growth
―Microgravity at International Space Station and 1G Conditions―

○Velu NIRMAL KUMAR, Mukannan ARIVANANDHAN, Govindasamy RAJESH, Tadanobu KOYOMA, Yoshimi MOMOSE (Shizuoka Univ.), Yuko INATOMI, Kaoruho SAKATA, Takehiko ISHIKAWA, Masahiro TAKAYANAGI, Shigeki KAMIGAICHI (JAXA), Tetsuo OZAWA (Shizuoka Inst. Sci. Tech.), Yasunori OKANO (Osaka Univ.), Yasuhiro HAYAKAWA (Shizuoka Univ.)

1. Introduction

InGaSb, a ternary alloy semiconductor having tunable lattice constant and wavelength ranging 6.096 ~ 6.479 Å and 1.7 ~ 6.8 μm is a potential material for thermo photovoltaic and IR detector applications[1]. Since the high temperature solution growth process is affected by solute convection on earth, it is important to understand the growth kinetic due to solute and heat transport. Microgravity is an ideal condition to study growth kinetics of crystals due to the suppression of convection. In the present study, we have grown InGaSb crystals under microgravity at International Space Station as well as on earth and investigated the effect of gravity on the growth.

2. Experiment

The growth experiments were carried on earth and microgravity conditions by vertical gradient freezing method using the sandwich structure of sample GaSb(seed)/Te-doped InSb/GaSb(feed). Prepared sample was heated at around 700 ˚C with temperature gradient 0.6 ˚C/mm and heat pulses at 2 h interval were applied to measure the growth rate. The grown crystals were cut along (110) plane after taking Laue pattern. Cut crystals were mirror polished and analyzed by electron probe micro analysis (EPMA). The growth striations were revealed by etching with 1:3:1 ratio of HF : $KMnO_4$: CH_3COOH for 30 min. at room temperature.

3. Results and discussions

Fig. 1 (a) shows indium composition profile of InGaSb crystals grown under microgravity and on earth. It revealed gradual decrease of indium composition along growth direction owing to shift in growth interface towards high temperature feed region. Dissolution of seed on earth (4.9 mm) was larger than microgravity (2.3 mm) due to strong convection and it is in agreement with the numerical simulations[2]. EPMA mapping in Fig. 1 (b) revealed that the growth interface shape was flat under microgravity and curved concavely towards feed in the earth grown sample. It conformed the dominant melt convection on earth and convection free growth under microgravity.

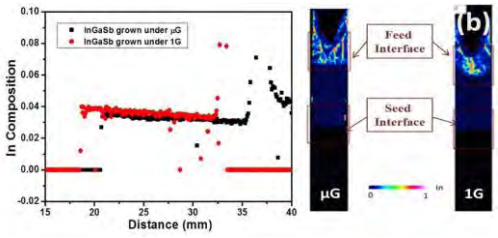

Fig. 1 (a) Indium composition profile and **(b)** indium mapping of microgravity and earth grown samples.

The observed growth striations (marked with red lines for clear visibility) of microgravity and earth grown samples are shown in Fig. 2(a) and (b). It also revealed that the shape of growth interface was almost flat in microgravity sample whereas it was concavely curved in earth grown sample owing to solution convection at higher temperature. The maximum growth rate was calculated to be 0.149 and 0.103 mm/h for InGaSb crystal grown under microgravity and on earth, respectively.

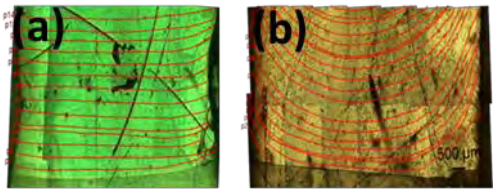

Fig. 2 Growth striations of **(a)** microgravity and **(b)** earth grown samples

References

1) P. S. Dutta, H.L. Bhat and V. Kumar: J. Appl. Phys., **81** (1997) 5821.

2) M. Nobeoka, Y. Takagi, Y. Okano, Y. Hayakawa and S. Dost: J. Crystal Growth, **385** (2014) 66

温度差マランゴニ効果による自由液膜内対流 -液膜形状が基本対流場に及ぼす影響-

○費　林昊（東理大院学），金子　敏宏（東理大），上野　一郎（東理大）

Effect of Static Deformation on Basic Flow Patterns in Thermocapillary-Driven Free Liquid Film

○Linhao Fei[1], Toshihiro KANEKO[2, 3], Ichiro UENO[2, 3]

[1]Div. Mechanical Engineering, Graduate School of Science & Technology, Tokyo Univ. Science

[2] Dept. Mechanical Engineering Fac. Science & Technology, Tokyo Univ. Science

[3] Research Institute for Science & Technology (RIST), Tokyo Univ. Science

1. Introduction

Fluid has in general negative temperature coefficient of surface tension; the fluid over the free surface is driven from a higher-temperature region to a lower-temperature region. In the case of a thin free liquid film with two free surfaces, however, a unique flow pattern is realized. Dr. Donald R. Pettit, a NASA astronaut, demonstrated a series of experiments in the International Space Station in 2003[1]. Among the fabulous demonstrations, he prepared a thin liquid film of water in a ring made by metal wire, and placed a heated iron close to one edge of the film. What he realized was that the fluid was driven in the film toward the heated iron, that is, from a colder region to a hotter region (Fig. 1). After this demonstration, there had been discussion on the mechanism of such a unique fluid motion. Ueno & Torii [2] demonstrated the thermocapillary-driven flow in a rectangular thin free liquid film in the terrestrial experiments. They indicated that there exist two major basic flows as a function of the shape of the liquid film in terms of aspect ratio by preparing a quite thin liquid film less than 1 mm in thickness to prevent the breakage of the film due to the normal gravity. The direction of the net flow, however, was from the hotter end to the colder one as generally expected.

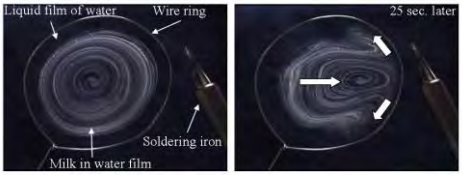

Fig. 1 Experiments on fluid dynamics by Dr. Donald Roy Pettit[1]. The fluid in a thin free liquid film is driven toward the heated area.

In 2010, Ueno et al.[3] firstly indicated by their experiments that the direction of the net flow by thermocapillary-effect in a rectangular thin liquid film is governed by the volume ratio of the film. In the case of the “fat” film, the direction is from the colder end to the hotter end, which corresponds to the result by Dr. Pettit. In the case of “thinner” film, on the other hand, the fluid is driven toward the colder end as indicated numerically by Kawamura et al.[4], and as indicated experimentally[2]. Recently, the effect of the volume ratio was numerically investigated by Yamamoto et al. in 2013[5]; they proposed that the direction of the net flow is governed by the vortex shape near the hot-end region.

The flow structures inside the film, however, have never been experimentally indicated because of the unique target geometry with deformation free surface. In order to understand the mechanism how the fluid chooses the direction of the net flow, there is no doubt that the information of the flow structures inside the film is indispensable. In the present study, we focus on the flow structures of the thermocapillary convection in a cross section normal to the end walls. We will present our latest results of our measurements in the poster.

2. Experimental Setup

Figure 2 represents the target geometry of the thin free liquid film, and apparatus in the present study. A liquid film is formed in a rectangular hole in the middle of a glass plate. A designated constant temperature difference ΔT is added to both end walls.

A thin liquid film of designated volume V is formed inside the hole. The 6-cSt silicone oil of 83 in Prandtl number (at 25 °C) is employed as the test fluid. The shape of the liquid film is described with three parameters[3], that is, the aspect ratios $\Gamma_x = L_z/L_x$ and $\Gamma_y = L_x/d$, and the volume ratio V/V_0, where L_x, d and L_z are the lengths in x, y and z direction, respectively, and V_0 is the volume of the hole $L_x d L_z$. We prepare two kinds of the plate; 0.6 mm and 0.2 mm in thickness. We define the Marangoni number $Ma = |\sigma_T|\Delta T d^2/\rho\upsilon\kappa L_x$ in order to indicate the intensity of the thermocapillary effect.

We monitor the surface temperature variation with the infrared (IR) camera, and the static profile of the film with the laser displacement sensor. In order to visualized the flow patterns, florescent particles of 13 μm in diameter are dispersed in the fluid of the film. The flow pattern in x-z plane is integratedly detected through the bottom free surface of the film by the whole illumination, and the pattern in x-y plane as the cross-sectional view is detected through the side wall of the plate. We prepare the laser light sheet of 0.3 mm in thickness to detect the cross-sectional view.

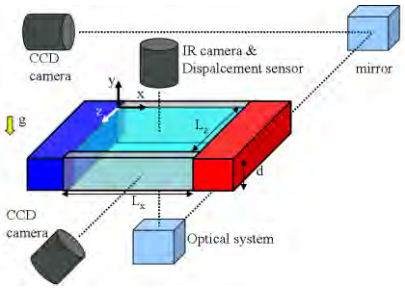

Fig. 2 Target geometry: a free liquid film exposed to a temperature gradient

2. Results and Discussion

In the present abstract, we focus on the results in the case of the liquid film in the plate of 0.6 mm in thickness, and (Γ_x, Γ_y) = (2, 3.33). The temperature difference ΔT is fixed at 6 K, which corresponds to Ma = 1.8×10^2. Under this condition, the flow patterns realized in the film exhibit a transition from "single-layered" flow to "double-layered" flow by varying the volume ratio[4].

Figure 3 indicates the results in the case of $V/V_0 = 0.75$. This figure consists of (a) the snapshot of the surface temperature obtained by the IR camera, (b) typical example of the particle path line observed from beneath (exposure time: 1.5 s), (c) profiles of the liquid film along x direction at different z, and (d) the typical example of the cross-sectional view of the particle path line in x-y plane at z = 2 mm (the center line) (exposure time: 1.5 s). In the frames of (b) and (d), arrows are added in order to illustrate the direction of the convection. As the Prandtl number of the test liquid is high, the temperature field is quite concurrent with the convective field. From the IR image and the particle path line observed from beneath, a single-layered flow is realized as observed by Ueno & Torii [3]; that is, a pair of vortexes exists in the span-wise direction. The vortexes are symmetrical with respect to the center line along the x direction. The fluid flows from hot wall to cold wall in the middle of the film along the center line. Frame (c) indicates that the profiles do not change drastically in x-y plane at different z. And, the convection under this condition does not affect the profile along x direction. From frame (d), the structure of convective field in x-y plane at z = 2 mm is clearly observed. Fluid comes into x-y plane along z direction near the hot wall. Then it flows from hot wall to cold wall over the free surfaces, rolling and turning sideward along z direction near the cold wall. A pair of vortexes exists in x-y plane near the cold wall to form double-layered structure in the depth direction. In the region near the hot wall, on the other hand, a "single-layered" structure is formed. It is firstly revealed that the so-called "single-layered" flow defined by Ueno & Torii [3] consists of two major regions along the center line.

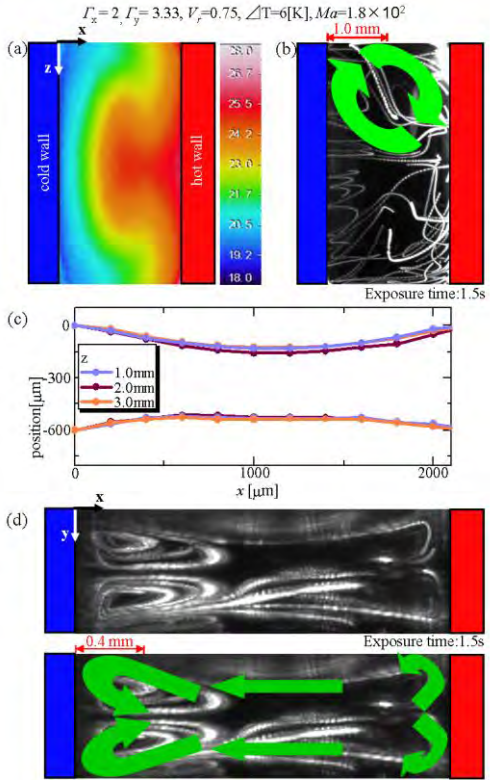

Fig. 3 Experimental results for (L_x, d, L_z) = (2 mm, 0.6 mm, 4 mm) under V/V_0 = 0.75: (a) snapshot of the temperature of the top surface by IR camera, (b) particle path lines for 1.5 s observed from beneath, (c) profiles of liquid film and (d) particle path lines obtained from the side. Noted that all results are obtained in a single experiment run but not-simultaneously.

Flow patterns change with aspect ratio and volume ratio. We will discuss with more results by varying these parameters in the poster.

4. References

1) http://science.nasa.gov/headlines/y2003/25feb_nosoap.htm

2) I. Ueno & T. Torii: Acta Astronautic, **66** (2010) 1017-1021.

3) I. Ueno, T. Katsuta & T. Watanabe: Proc. 2nd European Conf. on Microfluidics, **12** (2010) 1-9.

4) H. Kawamura, K. Iwamoto and M. Harashima: Journal of the Japan Society of Microgravity Application, **23** (2006) 157-160

5) T. Yamamoto, Y. Takagi, Y. Okano and S. Dost: Phys. Fluids, **25** (2013) 082108.

P20

水平円形伝熱面を用いた気泡微細化沸騰と伝熱面内温度分布の関連性について

○堀内和菜（東理大），安藤洵（東理大院），金子敏宏（東理大），上野一郎（東理大）

Correlation of Microbubble Emission Boiling on a Horizontal Circular Plate with Temperature Distribution of Heating Surface

○Kazuna HORIUCHI[1], Jun ANDO[2], Toshihiro KANEKO[1, 3], Ichiro UENO[1, 3]

[1]Dept. Mechanical Engineering Fac. Science & Technology, Tokyo Univ. Science

[2]Div. Mechanical Engineering, Graduate School of Science & Technology, Tokyo Univ. Science

[3]Research Institute for Science & Technology (RIST), Tokyo Univ. Science

1. Introduction

Recently, many people have requested improvement of cooling devices for developing highly-compacted and highly efficient electric devices. Boiling heat transfer with a liquid-vapor phase change accompanying a latent heat has been attracting rising attention because it indicates higher heat flux than the one that of single-phase cooling device. Under μg condition, however, heat-transfer efficiency drastically decreases because of the effect of derived vapor stagnating on the heating surface[1)]. A unique phenomenon named microbubble emission boiling (MEB) [2)] has been introduced to solve this problem. The MEB is a regime of the subcooled boiling in which the heat flux exceeds the upper limit of the heat flux, called critical heat flux (CHF), accompanying emission of the microbubbles of the order of 10^{-6} m in radius from heating surface. By the reasons stated above, the MEB is as a potential phenomenon for cooling devices under μg conditions. Although a number of experiments [e.g. 3, 4)] have been conducted to indicate its occurring conditions and the heat transfer coefficient, the mechanism itself of realizing high heat flux has not been elucidated clearly yet.

In this study, we have conducted experiments focusing on the correlation of the MEB on a horizontal circular plate. We especially focus on the uniformity of the boiling regimes over the heating surfaces of different size.

2. Experimental apparatus

Figure 1 shows a schematic view of the experimental apparatus. The copper block with a cylindrical rod is heated by cartridge heaters. The copper-rod surface is the test section. In prior to the series of experiments, we sanded the heating surface by using emery papers of #1000 to unify its roughness. After that, we cleaned the copper block using acetone. The block is installed the bottom of the test chamber, the surface of the copper rod only exposed to the test fluid. The chamber is partially filled the distilled water as the test fluid. The cooling channel made of copper was installed in the test fluid in order to define the degree of subcooling. The temperature distribution was measured in the preliminary experiments in order to convince ourselves that a designated temperature is realized far apart the heating surface. The degree of subcooling was defined by using that temperature. The diameter of the heating surface (ϕ) is 5, 10 and 15 mm. Four thermocouples are placed in the copper block, three of them are placed along the center of the block. Each thermocouple is positioned at 1, 3 and 5mm from the surface of the rod. The other is placed at 1-mm depth from the heating surface and 1-mm depth from the side wall of the copper rod. The temperature and the heat flux on the heating surface are evaluated from the temperatures along the center line of the rod using Fourier's law under assumption of one-dimensional steady heat conduction. The behavior of the vapor bubbles on the heating surface is tracked by using a high-speed camera with a frame rate up to 30,000 fps under a back-lighting system.

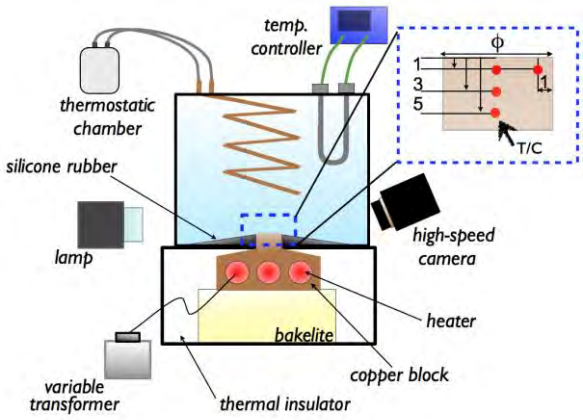

Fig. 1 Experimental apparatus

3. Results and discussion

3.1 Boiling curve

Figure 2 indicates the boiling curves in the case of ϕ = 10 mm. Under the condition ΔT_{sub} = 0 and 10 K, after the heat flux reaches the CHF point, a significant "jump" of the wall superheat emerges and the heat flux decreased drastically to realize the film or transient boiling. On the other hand, under

the condition $\Delta T_{sub} \geqq 20$ K, even though the heat flux reaches CHF, heat flux is not decreasing but increasing with the wall superheat. This regime is called "MEB," and a typical example of the vapor bubbles' behavior over the heating surface is shown in Fig. 3 .In this regime, smaller vapor bubbles cover the surface and violently bounce up and down over the surface. Such a bouncing of the vapor bubbles is always accompanied by the MEB.

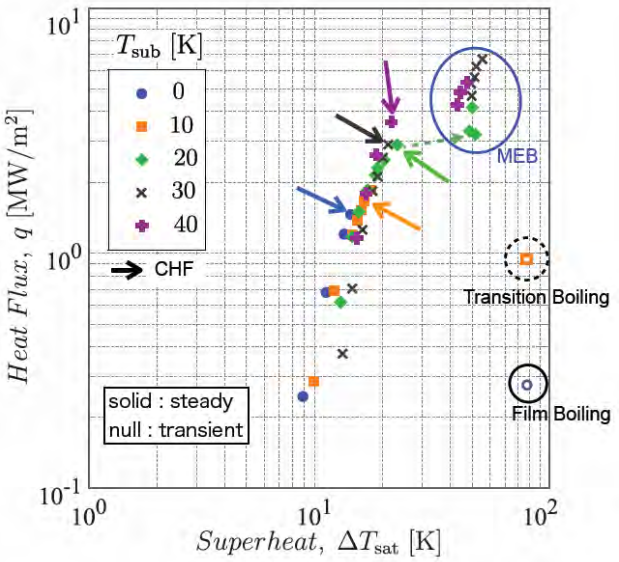

Fig. 2 Boiling curve under ΔT_{sub} = 0, 10, 20, 30 and 40 K with the boiling on the heating surface of 10 mm in diameter. Each point except null ones plot when temperature becomes steady. Dashed arrow represent significant jump of temperature under ΔT_{sub} = 20 K.

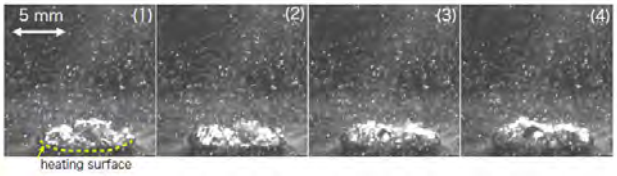

Fig. 3 Successive images of the MEB under ΔT_{sub} =30 K and q= 5.46 MW/m^2. Frame interval Δt= 4 ms and the shutter speed = 1/10000 s.

3.2 Behavior of vapor bubbles

Under the condition near the CHF point, the vapor forms coalesced bubbles covering the almost of whole area of heating surface. (Fig. 4(a)) From Fig. 4(a') which shows zoomed pictures of Fig. 4(a), one can find that the liquid-solid contact actively remains near the edge of the heating region because of the existence of nucleate boiling.[5] Then, we assume that there might be two regions on the heating surface with different boiling regimes. In this study, we take note of temperature distribution of the heating surface in the MEB region.

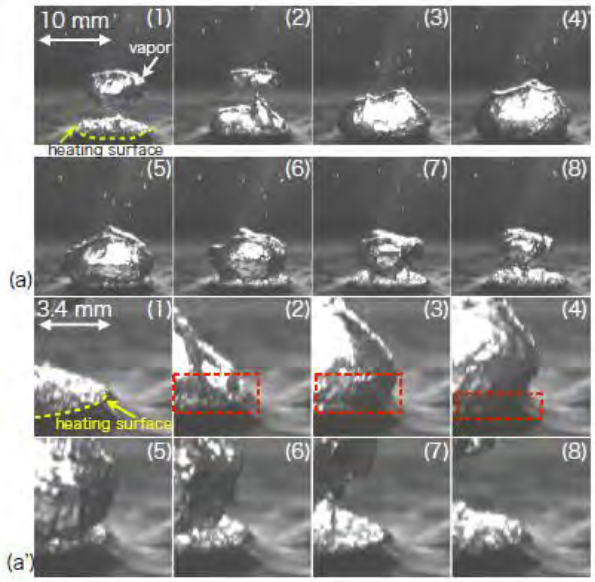

Fig. 4 (a) Successive images of the condensing vapor bubbles on the heating surface under ΔT_{sub} =30 K and q = 4.67 MW/m^2. Frame interval Δt = 35 ms and the shutter speed = 1/10000 s. Frame (a') indicates zoomed view of the right heating surface of (a).

Summary

・Experimental study on the microbubble emission boiling in a pool is conducted by focusing on the bubble behaviors and the heated surface.

・The MEB occurs under the condition $\Delta T_{sub} \geqq 20$ K. During this regime, the vapor bubbles on the heated surface bounce up and down with shooting out microbubbles in all directions. After the onset of MEB, The heat flux increase with the wall superheat.

・From the observation on the heating plate, we assume that there is the coalesced bubble near the center, while the nucleate boiling still activity at the edge of the surface.

References

1) J. Kim, J. F Benton and D. Wisriewski: Int. J. Heat Mass Trans., **45**, 19 (2002) 3919

2) S. Inada, Y. Miyasaka, S. Sakamoto and G. R. Chandratilleke: J. Heat Trans., **108**, 1 (1986) 219.

3) S. Kumagai, R. Kubo and T. Kawasaki: Heat Transfer-Asian Research, **32**, 2 (2003) 130.

4) G. Wang and P. Cheng: Int. J. Heat Mass Trans., **52** (2009) 79.

5) T. Saiki, T. Osawa, I. Ueno and C. Hong: Proc. the ASME 2013 Int. Tech. Conf. and Exh. (2013) 1